Master thesis

Topological Localized States in Excitable Delayed Systems

Submitted by

Leon Munsberg

May 11, 2019

First examiner
Priv.-Doz. Dr. Svetlana Gurevich

Second examiner
Prof. Dr. Uwe Thiele

Westfälische Wilhelms-Universität Münster
Fachbereich Physik
Institut für theoretische Physik

Contents

1 Introduction **1**

2 Theoretical Background **2**
2.1 Excitable Systems 2
2.2 Delay in Complex Systems and Quasi Continuous Spectrum of Eigenvalues 3
2.3 Floquet Theory and Stability of Periodic Solutions 5
2.4 Principle of Continuation 6
2.5 Dde-Biftool 7
2.6 From Class A Laser Equation to Delayed Adler Equation 8

3 Analysis of Delayed Adler Equation **11**
3.1 Steady States and their Stability 11
3.1.1 Continuation of Hopf Instability and Approximation of Discrete Eigenvalues 15
3.2 Periodic Orbits / Localised States 18
3.2.1 Antikinks 21
3.2.2 Continuation of Bifurcations in Δ-ψ Plane 23
3.2.3 Properties of Localized States 27
3.2.4 Connection with Steady State / Emergence 31
3.3 Interaction between Localised States 36
3.3.1 Locking 45
3.3.2 Multiple Localised States 49
3.3.3 Kink-Antikink Interaction 50

4 Conclusion and Outlook **51**

References **53**

Acknowledgements **57**

Declaration of Academic Integrity **59**

1 Introduction

Localized structures occur in a variety of complex systems mainly in the from of pulses or fronts, naming surface solitons on magnetic fluids [1] and vegetation patterns [2] as two examples. In non conservative systems they are often called dissipative solitons [3] and share some similarity with classical solitons [4] in conservative systems. While classical solitons require a balance between dispersion and nonlinearities in order to be stable, dissipative solitons require an additional balance of energy gain and loss. Classical solitons are mostly part of a family of solutions, however the additional restriction to dissipative solitons leads to solitary solutions with fixed properties.
While there are spatial localized structures, naming soliton waves in water channels [5] as one example, there is also the possibility for temporal localized states (LSs) that can for example occur in mode locked laser systems [6]. While spatial LSs are solutions of partial differential equations (PDE), temporal LSs can often be observed in time-delayed systems as shown in [7] and [8]. In fact there is a certain similarity relating time-delayed systems and spatially extended system as discussed in [9].
While LSs in optical systems can appear in the form of intensity pulses [10], the possibility of creation of temporal LSs in the phase of the light was shown in [11]. In contrast to dissipative solitons, which gain their robustness through a balance of dispersion and nonlinearity provided by e.g. the Kerr effect in addition to a balance of gain and loss, the observed phase objects consist of 2π phase rotations that obtain their robustness through the topological nature of the phase space.
In particular, temporal LSs have sparked an interest in regenerative memories since their robustness allows for storage of information within an optical cavity as seen in [8]. Especially the formation of localized structures in semiconductor laser systems is of interest because optical data transmission already relies heavily on optical semiconductor devices.
In this thesis we investigate the existence of temporal LSs in a phase model that exhibits excitation as well as time-delayed feedback. Instead of a in depth model describing the time evolution of an electric field, gain and loss in a passively mode locked semiconductor laser, as derived in [12], we examine a simpler model describing the phase of an injection locked semiconductor laser. This model was derived in [11] and is called the delayed Adler equation. After an introduction of the theoretical background in chapter 2 we study the existence of LSs in the delayed Adler equation, in chapter 3. Starting with the steady states, forming the background for the localized solutions, in section 3.1 we introduce a periodic solution as a reappearing 2π phase excitation in section 3.2. After briefly discussing the existence of negative excitations of -2π in section 3.2.1 we continue with numerical continuation and bifurcation analysis of the periodic solution in 3.2.2. The following section 3.2.3 discusses the idea of localization in the context of the observed periodic solutions and introduces a measure describing their width in order to determine if the concept of localization is applicable to them. Section 3.2.4 then discusses the connection of the steady state and the periodic solution revealing a global bifurcation. Since more than one LS can be present in the system section 3.3 explores the interaction between LSs. A reduced model is derived describing the movement of the centers of two interacting LSs and the results are compared to the results obtained by means of direct numerical simulations.

2 Theoretical Background

In this chapter we will introduce the necessary background needed to investigate the system which is subject of this thesis. Starting with section 2.1 the general principle of excitability will be explained without the additional complexity of time delay. The following section 2.2 will then focus on systems under the influence of time-delayed feedback in general and the properties of such systems. Section 2.3 will then introduce the principles of Floquet theory and the stability of periodic solutions in dynamical systems. The main tool used to perform the bifurcation structure of delayed differential equations is `dde-biftool` and we discuss its methods briefly in section 2.5. Section 2.6 describes an experiment exhibiting localised structures in an excitable delayed system and the derivation of a simple model to describe them.

2.1 Excitable Systems

Excitability is a concept which can be observed in many systems in different fields. It involves the ability of a system to amplify a small perturbation of a state followed by a refractory period needed to reset the system to the original state. In this refractory period another excitation can not take place. Examples would be the excitation of neurons where a slight increase in membrane potential starts a process leading to a further increase in potential and finally the depolarization of the membrane. In a spatially extended system this excitation at one point can trigger the excitation at neighbouring points leading to the propagation of a wave. In neurons this allows the signal transmission in our neural system, which was studied in detail by [13]. In [14] the phenomenon of a forest fire was modeled by an excitable system, where the fire itself corresponds to the excitation and the regrowth of the forest was considered the refractory period.

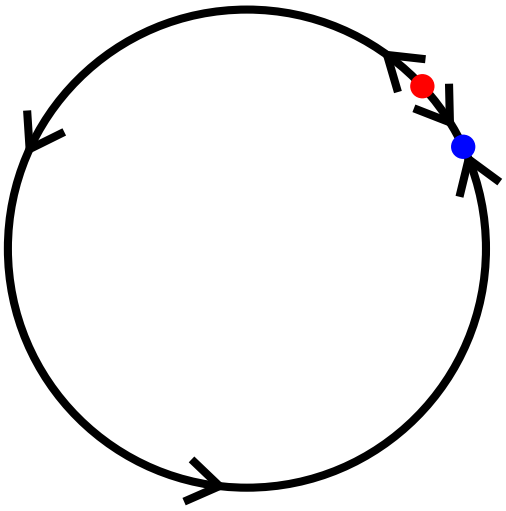

Figure 2.1.1: Flow of the phase θ given by eq. (2.1.1) on a circle. The blue and red dot show stable and unstable fixed points.

Another mechanical example, that can be described in a simpler mathematical model, describes the weak coupling of two oscillators with a small detuning Δ in their frequencies. In this case one can derive the so called Adler equation [15]

$$\frac{\mathrm{d}\theta}{\mathrm{d}t} = \Delta - \sin(\theta) \tag{2.1.1}$$

describing the phase difference between both oscillators. This is the simple case of two oscillators in the general Kuramoto model [16], describing the synchronization of multiple weakly coupled oscillators. In particular for values of $\Delta \in [-1, 1]$ the system has fixed points, where $\frac{\mathrm{d}\theta}{\mathrm{d}t} = 0$ corresponding to solutions in which both oscillators have a fixed phase difference. However, for $\Delta \neq 0$ one of the oscillators always lags behind and outside of the stable regime the phase difference periodically does a full rotation so that the slower oscillator can keep up with the faster one. This phase rotation can also be the result of a small perturbation inside the stable regime resulting in a behavior that can be called an excitation.

This behavior is further illustrated in fig. 2.1.1 in which the flow of the phase field θ is displayed in a circle, since θ represents a phase difference and is therefore 2π periodic. The arrows show the direction of $\frac{\mathrm{d}\theta}{\mathrm{d}t}$ and the blue and red dot represent the stable and unstable steady states. The system is close but bellow the critical point $\Delta = 1$, so that the two fixed points are nearby. If the system is now in the stable fixed point (blue dot), a small perturbation would be enough to get beyond the unstable fixed point (red dot) which would result in a full rotation along the circle back to the initial stable fixed point. This resulting orbit is much longer than the initial perturbation which fits the concept of excitability. Additionally a perturbation during the orbit back to the stable fixed point does not lead to another excitation which illustrates the idea of a necessary refractory period.

2.2 Delay in Complex Systems and Quasi Continuous Spectrum of Eigenvalues

Delay differential equations (DDEs) are systems of differential equations where the governing equation does not solely depend on the present state $\phi(t)$ of the system and a set of control parameters μ but additionally include a past state of the system $\phi(t-\tau)$

$$\frac{\mathrm{d}\phi(t)}{\mathrm{d}t} = f(\phi(t), \phi(t-\tau), \mu), \tag{2.2.1}$$

where $f(\phi(t), \phi(t-\tau), \mu)$ represents a function governing the systems dynamics. In more complex situations there can be multiple delays $\phi(t-\tau_i)$, nonlocal dependency on a time interval $\int_{t-\tau}^{t} \phi(t)\mathrm{d}t$ or even state dependent delays $\phi(t-\tau(\phi(t)))$. However this chapter will only focus on delay systems with one single fixed delay.

One key difference between DDEs and ordinary differential equations (ODE) is the amount of initial conditions needed to predict the time evolution of the system. In deterministic ODE systems all information needed to predict the time evolution of a initial state $\phi(t_0)$ lies in the state at one point in time. For DDEs a complete prediction of the future of the system requires not only the state $\phi(t_0)$ at one point but also the complete past of the system up to the point $\phi(t_0 - \tau)$ [17]. Similar to partial differential equations (PDE) describing the dynamics of spatially extended systems, the initial condition is now a function on a defined interval: $\phi(t); t \in [t_0 - \tau, t_0]$ for DDEs and $\phi(t_0, x); x \in [0, L]$ for a PDE defined on an interval of length L, resulting in infinitely many degrees of freedom. A detailed investigation on the relationship between DDEs and PDEs can be found in [9].

For the calculation of steady state solutions ϕ_{st} of eq. (2.2.1) the additional dependency on the delayed state is not problematic because the steady state should not change over time $\phi(t) = \phi(t-\tau) = \phi_{\mathrm{st}}$ and can be determined by $f(\phi_{\mathrm{st}}, \phi_{\mathrm{st}}, \mu) = 0$. The linear stability analysis however is a bit more involved. When considering a small perturbation $\phi_{\mathrm{st}} + \epsilon$, $\epsilon \ll 1$ and assuming ϕ evolves in the form $\phi(t) = \phi_{\mathrm{st}} + \epsilon e^{\lambda t}$, equation (2.2.1) can be linearised in ϵ. This leads to the eigenvalue problem for the eigenvalues λ of the steady state

$$\epsilon\lambda e^{\lambda t} = \frac{\partial f(\phi(t), \phi(t-\tau), \mu)}{\partial \phi(t)} \epsilon\lambda e^{\lambda t} + \frac{\partial f(\phi(t), \phi(t-\tau), \mu)}{\partial \phi(t-\tau)} \epsilon\lambda e^{\lambda(t-\tau)}$$

and can be rearranged to the characteristic equation

$$\lambda = A + Be^{-\lambda\tau}, \tag{2.2.2}$$

$$A = \left.\frac{\partial f(\phi(t), \phi(t-\tau), \mu)}{\partial \phi(t)}\right|_{\phi_{\mathrm{st}}}, \tag{2.2.3}$$

$$B = \left.\frac{\partial f(\phi(t), \phi(t-\tau), \mu)}{\partial \phi(t-\tau)}\right|_{\phi_{\mathrm{st}}}, \tag{2.2.4}$$

which is a transcendental equation and can in general not be solved analytically. Furthermore there are infinitely many solutions of this equation leading to an infinite number of eigenvalues even for one-dimensional systems with a single delay term. This can again be seen as a similarity between DDEs and PDEs since the spacial extension of an ODE also leads to infinitely many eigenvalues each corresponding to a spatial mode existing in the system.
However, for specific parameter sets one can calculate the eigenvalues analytically using the implicit Lambert W functions [18] which are defined as the inverse of the function $f(z) = ze^z$. Since f is not injective there are multiple branches denoted $W_n(ze^z) = z$. For real-valued z there only exist solutions for $z \geq -\frac{1}{e}$ namely the principle branch W_0, starting at $W_0\left(\frac{1}{e}\right) = -1$ and passing $W_0(0) = 0$, in addition to a second branch denoted W_{-1} which only exists in $z \in \left(\frac{1}{e}, 0\right]$ and branches of at $W_{-1}\left(-\frac{1}{e}\right) = -1$ diverging to $W_{-1}(0) = -\infty$. For complex-valued z there are countably many solutions corresponding to the branches W_n. While the Lambert W functions can not be expressed in elemental functions they are well studied and can be numerically calculated. Using the Lambert W functions solutions of eq. (2.2.2) can be found in the form:

$$\lambda_n = \frac{1}{\tau}\left(A\tau + W_n\left(B\tau e^{-A\tau}\right)\right). \tag{2.2.5}$$

While there are infinitely many discrete eigenvalues solving the characteristic equation they all lie on a so called pseudo-continuous spectrum as shown in [19]. In long delay systems it is possible to approximate this pseudo-continuous spectrum in order to get a comparably simple relation between the real and imaginary part of the eigenvalues λ_n. By splitting the eigenvalues in the form of $\lambda = \frac{\alpha}{\tau} + i\beta$ and inserting in to the characteristic equation (2.2.2) while only considering the leading order in $\frac{1}{\tau}$ one can derive the following relation:

$$\alpha = \frac{1}{2}\ln\left(\frac{B^2}{A^2 + \beta^2}\right), \tag{2.2.6}$$

which is called the long delay limit. If one observes the exact set of discrete eigenvalues λ_n with increasing delay τ, the distance between the eigenvalues in the complex plane decreases. This leads to more eigenvalues in the vicinity of the dominant eigenvalue with the maximum real part and essentially increases the number of relevant degrees of freedom [20]. If one considers the limit of $\lim_{\tau\to\infty}$ the distance between the eigenvalues converges to 0, which effectively fills the complete pseudo continuous spectrum with discrete eigenvalues λ_n.

2.3 Floquet Theory and Stability of Periodic Solutions

Periodic solutions are time dependent solutions $\phi(t)$ of a dynamical system

$$\frac{\mathrm{d}\phi}{\mathrm{d}t} = f(\phi, \mu) \tag{2.3.1}$$

that return to their initial state after a fixed period of time T, such that $\phi(t+T) = \phi(t)$. The analysis of their stability is more involved than for fixed points so the basic tools for describing stability of periodic solutions, namely the monodromy matrix and Floquet multipliers, will be introduced in this section [21].
Let $\phi(t, z)$ be a periodic solution of a system in the form of eq. (2.3.1) with initial condition $\phi(0) = z$, then the stability of this solution can be described by the behavior of neighboring solutions $\phi(t, z+\epsilon)$. If the distance between the two trajectories $d(t) = \phi(t, z) - \phi(t, z+\epsilon)$ diverges, the initial solution is regarded as unstable and if it converges to 0 the solution $\phi(t, z)$ is stable. For small perturbations ϵ one can linearise the distance after one period as

$$d(T) = \frac{\partial\phi(T, z)}{\partial z}\epsilon + \mathcal{O}(\epsilon^2).$$

In the general case of a n-dimensional system with solution $\phi_i(t, z_i)$ and initial conditions $\phi_i(0) = z_i$ the linear term is given by a $n \times n$ matrix

$$M = \frac{\partial\phi(T, z)}{\partial z}$$

which is called the monodromy matrix. The eigenvalues μ_i, which are called Floquet multipliers, and the corresponding eigenvectors govern the stability of the periodic solution $\phi(t, z)$. If one or more eigenvalues lie outside the unit circle ($|\mu_i| > 1$) the solution is unstable, whereas if every eigenvalue lies inside the unit circle the solution is stable. However it can be shown that each autonomous system has at least one eigenvalue $\mu_i = 1$ belonging to the translation along the periodic orbit. For any phase shift ζ the solution $\phi(t+\zeta)$ is a periodic solution with the same behavior as $\phi(t)$. In the context of neighboring trajectories this implies that there is a perturbation $\epsilon = \phi(\zeta) - \phi(0)$ leading to a shifted periodic orbit with the same period. Since the distance between those orbits does not change over one period the corresponding eigenvalue to this perturbation is $\mu_i = 1$.
In order to calculate the monodromy matrix, one can differentiate the dynamical system (2.3.1) with respect to the initial condition z leading to

$$\frac{\mathrm{d}}{\mathrm{d}t}\frac{\partial\phi(t, z)}{\partial z} = \frac{\partial f(\phi(t, z), \mu)}{\partial\phi(t, z)}\frac{\partial\phi(t, z)}{\partial z}.$$

Additionally one can identify

$$\frac{\partial\phi(0, z)}{\partial z} = \underline{1},$$

since $\phi(0, z) = z$. If the periodic solution $\phi(t, z)$ is known, one can now calculate the monodromy matrix M by solving the initial value problem for a new variable $\Phi(t) = \dfrac{\partial\phi(t, z)}{\partial z}$

$$\frac{\mathrm{d}\Phi(t)}{\mathrm{d}t} = \frac{\partial f(\phi(t, z), \mu)}{\partial\phi(t, z)}\Phi(t)$$

with an initial condition

$$\Phi(0) = \underline{1}$$

and identifying $M = \Phi(T)$. The calculation of the monodromy matrix and the Floquet multipliers was included in the `dde-biftool` which was used as the main computational tool in this thesis and is briefly described in section 2.5.

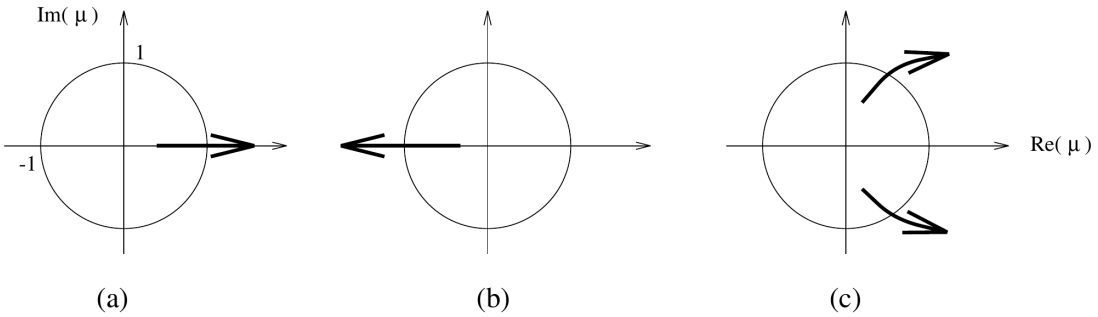

Figure 2.3.1: Different instabilities of a periodic solution by means of a one or more Floquet multipliers leaving the unit circle. (a): Floquet multiplier leaving the unit circle at $\mu = 1$ leading to a fold bifurcation. (b): Floquet multiplier leaving the unit circle at $\mu = -1$ leading to a period doubling bifurcation. (c): complex conjugate pair of Floquet multipliers leaving the unit circle leading to a torus bifurcation [21].

One can distinguish different types of instabilities of the periodic solution depending on how a Floquet multiplier leaves the unit circle [22]. If a Floquet multiplier reaches $\mu_i = 1$ as depicted in fig. 2.3.1 (a) the periodic solution undergoes a fold bifurcation resulting in a turning point in the bifurcation diagram.

A Floquet multiplier of exactly $\mu_i = -1$ as seen in fig. 2.3.1 (b) would lead to a small perturbation ϵ evolving to an opposite perturbation $-\epsilon$ after one period T. By changing the sign of the perturbation every period one essentially ends up with a solution of period $2T$ leading to a period doubling bifurcation or flip bifurcation. If higher order terms stabilize the perturbation beyond the bifurcation point a new branch of periodic solutions emerges.

The third bifurcation type is called a torus bifurcation and involves a pair of complex conjugate Floquet multipliers leaving the unit circle as seen in fig. 2.3.1 (c). It is similar to the period doubling bifurcation as an initial perturbation starts to oscillate, however the period of the perturbation is not necessarily a multiple of the period of the initial solution. The arising attractor forms a torus around the solution undergoing the bifurcation which gives it the name torus bifurcation. As period doubling bifurcations also inhibit periodic behavior of a perturbation, they can technically be classified as special torus bifurcations with a fixed ratio of periods. Therefore they also lead to tori around the initial solution but in this case they are flattened to the form of a mobius strip.

2.4 Principle of Continuation

Path-Continuation is a numerical method to follow both stable and unstable solutions in parameter space. In contrast to a direct numerical integration of one particular initial condition, it is possible to follow specific types of solutions and find bifurcation points, where the stability changes or new solutions emerge. If ϕ_0^* is a solution of the ODE

system

$$\frac{\mathrm{d}\phi}{\mathrm{d}t} = f(\phi, \mu) \tag{2.4.1}$$

at parameter μ_0^* one expects to find another solution ϕ_1^* when slightly changing the parameter to $\mu_1^* = \mu_0^* + \Delta\mu$. In fact both of those solutions lie on a continuous branch of solutions $\phi^*(\mu^*)$ which we would like to reveal with this method. Continuation now works in two steps at first a new point is predicted, for example with a tangent prediction:

$$\phi_{i+1}^* = \phi_i^* + \frac{\mathrm{d}\phi(\mu)}{\mathrm{d}\mu}\Delta\mu. \tag{2.4.2}$$

Afterwards the predicted point ϕ_{i+1}^* is corrected with a Newton algorithm to satisfy $f(\phi_{i+1}^*, \mu_{i+1}^*) = 0$, in case of a steady state, or a suitable condition in case of a periodic solution or bifurcation point. This approach however is bound to fail at turning points, where a branch $\phi^*(\mu^*)$ has a solution for a parameter μ^* but does not for $\mu^* + \Delta\mu$. In this case one could use a arclength predictor which does a step in the arclength

$$s = \int |\frac{\mathrm{d}\phi^*(\mu^*)}{\mathrm{d}\mu^*}|\mathrm{d}\mu^*$$

rather than the parameter μ^*. For small step lengths one arclength step Δs can be approximated by $\Delta s^2 = \Delta\phi^2 + \Delta\mu^2$. A more in depth description of the topic is available in [23] or [21].

2.5 Dde-Biftool

The `dde-biftool` is a set of routines dedicated to numerical bifurcation analysis of delayed differential equations that runs in Matlab or Octave. The version used in this thesis is 3.1.1 and can be obtained at https://sourceforge.net/projects/ddebiftool/. We will briefly describe the capabilities and structure of the tool in this section. Additional instructions can be found in the manual [24] and a more in depth description including examples is given in [23].
The `dde-biftool` is able to calculate steady state and periodic solutions by searching for roots of the system equation and follow these solutions in parameter space via arclength-path-continuation. The predictor method is a secant prediction with adaptive step length multiplying the step length by a constant factor larger than one on success. If the correction of a predicted point fails, a new point is predicted from a intermediate point between the last two successfully calculated ones, effectively dividing the step length by a factor two. While there is the option for different predictor methods, the secant prediction is currently the only choice.
In the case of time dependent solutions $\phi(t)$ of period T in delayed systems one has to account for the continuous profile of the state $\phi(t); t \in [t_0, t_0 + T]$ which has infinite degrees of freedom to be corrected by the continuation algorithm. In this case `dde-biftool` approximates the profile as a piecewise polynomial of degree d on a adaptive mesh with N points. One can completely describe this polynomial with additional intermediate mesh points

$$t_{i,j} = t_i + \frac{j}{d}(t_{i+1} - t_i),$$

where $i \in [0, N-1]$ is the index counting mesh points and $j \in [0, d-1]$ counts d additional intermediate points for every mesh point. This not only reduces the system

to $N \cdot d$ values $\phi_{i,j} = \phi(t_{i,j})$ instead of a continuous profile, but also makes it possible to interpolate $\phi(t_{i,j} - \tau)$ even if $t_{i,j} - \tau$ does not coincide with a mesh point.
In contrast to other popular continuation tools like AUTO [25] or pde2path [26], the stability is not calculated during continuation which makes automated bifurcation detection and branch switching impossible. However, one can compute the stability of obtained solutions in a separate routine. This has the advantage of decreased computation time since the calculation of stability can be quite time consuming especially for delay differential equations.
The structure of `dde-biftool` is divided into four layers starting with the lowest layer 0 in which the system is defined. This includes the differential equations themselves, additional conditions, the number of involved delays and optionally provided derivatives of the differential equations. All these have to be provided by the user and are saved in a single structure that will be used by the higher layers.
The second layer, layer 1, provides the numerical methods for continuation or determination of stability. This layer is not meant to be visible to the user but is accessed by the layers 2 and 3.
Layer 2 handles individual points in the system. A point can describe a solution of the system, namely steady states, periodic solutions and connecting orbits, or a bifurcation point, while only fold and Hopf bifurcations are supported in the original version. Depending on the type of point the matching numerical methods are provided by layer 1. In points involving time dependent profiles, a polynomial interpolation on an adaptive mesh is used. Here one can adjust the degree of the polynomial as well as the number of mesh points which opens the possibility to tune the algorithm between accuracy and speed. There are several functions that operate on points that can be used to calculate stability, correct a point or change the mesh of a profile. Those functions are also used by the last layer.
The actual continuation happens in layer 3. This layer operates on branches which are collections of multiple points. A minimal branch suitable for continuation has two successfully corrected points, a list of free parameters and the respective methods provided by layer 1. Functions operating on branches include continuation, calculation of stability, reversal of a branch and branch plotting. If a change of stability is found on a branch of solutions it is possible to manually convert a point in the vicinity of the stability change into an approximation of a bifurcation point. This new point can then be corrected and used to start the continuation of a new branch.
In addition to `dde-biftool`, the extension `extra_psol` [27] was used, which adds bifurcations of periodic solutions to the supported point types. This enables the continuation of fold, torus or period doubling bifurcations of periodic orbits.

2.6 From Class A Laser Equation to Delayed Adler Equation

While the concept of excitability and time delay can be found in many systems and fields of research there is one particular experiment inspiring this thesis. In [11] it was shown that operating an injection locked semiconductor laser in an excitable regime with delayed feedback can lead to temporally localised phase structures. It was experimentally shown, that multiple of those, so called phase bits can coexist in the system and can be individually addressed. Both the nucleation and the cancellation of individual phase bits was successfully shown and the storage of a 8-bit integer was demonstrated. In addition, a DDE for the phase difference between the slave and master laser for small injection and detuning was derived. Because the resulting equation is subject of this thesis we will recall the derivation shown in the supplementary material of [11].

Staring with the class-A laser equation of a injection locked laser with detuning Δ, linewidth enhancement factor α and injection amplitude Y that includes delayed feedback of strength η, phase Ω and time delay τ

$$\frac{\mathrm{d}E}{\mathrm{d}t} =(1+i\alpha)(1-|E|^2)E + Y + i\Delta E + \eta e^{-i\Omega}E(t-\tau) \tag{2.6.1}$$

one can split the electric field E in to amplitude ρ and phase ϕ, i.e. $E = \rho e^{i\phi}$ leading to

$$\frac{\mathrm{d}\rho}{\mathrm{d}t} =(1-\rho^2)\rho + Y\cos(\phi) + \eta\rho(t-\tau)\cos(\phi(t-\tau)-\phi-\Omega), \tag{2.6.2}$$
$$\frac{\mathrm{d}\phi}{\mathrm{d}t} =\alpha(1-\rho^2) + \Delta - \frac{Y}{\rho}\sin(\phi) + \eta\frac{\rho(t-\tau)}{\rho}\sin(\phi(t-\tau)-\phi-\Omega). \tag{2.6.3}$$

A multiple time scale expansion of the form

$$\rho =1 + \epsilon r(t_1,t_2) + \mathcal{O}(\epsilon^2), \tag{2.6.4}$$
$$\phi =\phi(t_1,\epsilon t_2), \tag{2.6.5}$$
$$\frac{\mathrm{d}}{\mathrm{d}t} =\frac{\partial}{\partial t_1} + \epsilon\frac{\partial}{\partial t_2}, \tag{2.6.6}$$

where t_1 represents the fast time scale, t_2 the slow time scale and ϵ the time scale separation, was performed. This leads to the following system of equations in the first order of ϵ

$$\frac{\partial r}{\partial t_1} =-2r + Y\cos(\phi) + \eta\cos(\phi(t-\tau)-\phi-\Omega) \tag{2.6.7}$$
$$\frac{\partial \phi}{\partial t_1} =0 \tag{2.6.8}$$
$$\frac{\partial r}{\partial t_2} =0 \tag{2.6.9}$$
$$\frac{\partial \phi}{\partial t_2} =-2\alpha r + \Delta - Y\sin(\phi) + \eta\sin(\phi(t-\tau)-\phi-\Omega) \tag{2.6.10}$$

in which the amplitude ρ does not depend on the slow time scale t_2 and the phase ϕ does not depend on the fast time scale t_1. This lets us eliminate the dynamics of the amplitude by adiabatic elimination [28] which leads to a fixed relation $r(\phi)$:

$$2r = Y\cos(\phi) + \eta\cos(\phi(t-\tau)-\phi-\Omega). \tag{2.6.11}$$

This expression inserted in equation (2.6.10) leads to a uncoupled equation for the phase ϕ:

$$\frac{1}{\sqrt{1+\alpha^2}}\frac{\mathrm{d}\phi}{\mathrm{d}t_2} =\frac{\Delta}{\sqrt{1+\alpha^2}} - Y\sin(\phi+\arctan(\alpha)) + \eta\sin(\phi(t-\tau)-\phi-\Omega-\arctan(\alpha)). \tag{2.6.12}$$

By rescaling the time and delay as $t' = Y\sqrt{1+\alpha^2}\,t$ and $\tau' = Y\sqrt{1+\alpha^2}\,\tau$, as well as the detuning $\Delta' = \Delta/(Y\sqrt{1+\alpha^2})$ and dropping the $'$ in t', τ' and Δ', while redefining the phase $\theta = \phi + \arctan(\alpha)$, the feedback phase $\psi = \Omega + \arctan(\alpha)$ and the feedback strength $\chi = \eta/Y$ one ends up with the delayed Adler equation:

$$\frac{\mathrm{d}\theta}{\mathrm{d}t} = \Delta' - \sin(\theta) + \chi \sin(\theta(t'-\tau') - \theta - \psi). \tag{2.6.13}$$

This is a scalar DDE with a single fixed delay τ and three additional control parameters. The properties of this equation will be discussed in detail in chapter 3.

3 Analysis of Delayed Adler Equation

The delayed Adler equation is a very simple model that exhibits both excitability and delay. It is also a general equation, that applies to many systems showing synchronisation and some form of small delayed feedback [29].

$$\frac{\mathrm{d}\theta}{\mathrm{d}t} = \Delta - \sin(\theta(t)) + \chi \sin(\theta(t-\tau) - \theta(t) - \psi) \tag{3.0.1}$$

Like in the Adler equation without delay (2.1.1), the quantity described by eq. (3.0.1) is the phase difference θ between two weakly coupled oscillators. There are only four parameters that influence the systems behavior including the delay time τ of the feedback. The other parameters are the detuning Δ between the oscillators, the strength χ of the delayed feedback and a additional phase ψ that is added to the feedback term. The state variable θ, as well as all the parameters present in eq (3.0.1), are one-dimensional real-valued quantities. The complexity of the dynamics arising from this model lies in the trigonometric nonlinearity and especially in the delayed feedback term.
In the following Chapter we will show that the two phenomena of delay and excitability can lead to the existence of localized structures using the example of the delayed Adler equation (3.0.1). First the steady states of the system will be examined to determine the background on which the localised structures arise. In section 3.2 periodic solutions are introduced and investigated while the localised nature of said periodic solutions is discussed in section 3.2.3.

3.1 Steady States and their Stability

The steady states of eq. (3.0.1) are defined by $\dfrac{\mathrm{d}\theta}{\mathrm{d}t} = 0$ while the delayed term satisfies $\theta(t-\tau) = \theta(t)$. Equation (3.0.1) then simplifies to:

$$0 = \Delta - \sin(\theta) - \chi \sin(\psi),$$

which is solved by:

$$\begin{aligned} \theta_s &= \arcsin(\Delta - \chi \sin(\psi)) + 2\pi n, && n \in \mathcal{Z}, \\ \theta_u &= \pi - \arcsin(\Delta - \chi \sin(\psi)) + 2\pi n, && n \in \mathcal{Z}. \end{aligned}$$

The linear stability analysis for the surroundings of the steady states $\theta_{s,u} + \epsilon$ yields the characteristic function:

$$\lambda = A + Be^{-\lambda\tau}, \tag{3.1.1}$$

where A and B are the coefficients of the linearised problem that read:

$$\frac{\mathrm{d}(\theta_{s,u} + \epsilon)}{\mathrm{d}t} = A\epsilon(t) + B\epsilon(t-\tau) + \mathcal{O}(\epsilon^2), \tag{3.1.2}$$

$$A = -\cos(\theta_{s,u}) - \chi\cos(\psi), \tag{3.1.3}$$

$$B = \chi\cos(\psi). \tag{3.1.4}$$

Note that without the delay term ($\chi = 0$) the eigenvalues $\lambda_{s,u}$ are given by:

$$\begin{aligned} \lambda_{s,u} &= -\cos(\theta_{s,u}), \\ \theta_s &\in \left[-\frac{\pi}{2}, \frac{\pi}{2}\right] + 2\pi n, && n \in \mathcal{Z}, \\ \theta_u &\in \left[\frac{\pi}{2}, \frac{3\pi}{2}\right] + 2\pi n, && n \in \mathcal{Z}, \end{aligned}$$

leading to $\lambda_s < 0$ and $\lambda_u > 0$. Therefore without delay θ_s is always stable and θ_u is always unstable.
For $\Delta = 1$ both steady states coincide at:

$$\theta_{s,u} = \frac{\pi}{2} + 2\pi n, \qquad n \in \mathcal{Z},$$

while for $\Delta = -1$ they coincide at:

$$\theta_{s,u} = \frac{3\pi}{2} + 2\pi n, \qquad n \in \mathcal{Z}$$

and disappear in a saddle-node bifurcation for $|\Delta| > 1$ as seen in fig. 3.1.1.

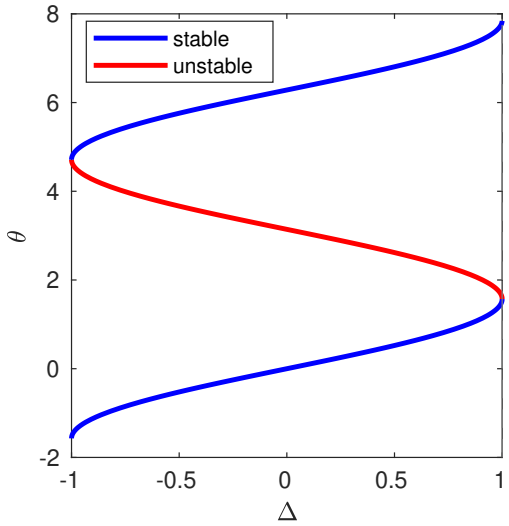

Figure 3.1.1: Stable and unstable steady states of eq. (3.0.1) without the delay term ($\chi = 0$).

Considering the influence of the delay the steady states only exist for:

$$\Delta - \chi \sin(\psi) \in [-1, 1]$$

leading to the boundaries:

$$\Delta = 1 + \chi \sin(\psi), \tag{3.1.5}$$
$$\Delta = -1 + \chi \sin(\psi) \tag{3.1.6}$$

effectively shifting the saddle-node bifurcation to higher values of Δ for $\psi \in [0, \pi]$ and to lower values for $\psi \in [\pi, 2\pi]$ while the maximum shift is given by χ.
The characteristic equation (3.1.1) can not be solved analytically for $\chi \neq 0$ because it is transcendental. However solutions for λ can be found using the Lambert W functions which solve $z = W_n(ze^z)$ as described in 2.2:

$$\lambda_n = \frac{1}{\tau}(A\tau + W_n(B\tau e^{-A\tau})). \tag{3.1.7}$$

The resulting number of eigenvalues is infinite because of the infinite number of branches of the Lambert W functions denoted W_n with $n \in \mathcal{Z}$.
In the limit of long delays the infinite number of eigenvalues accumulate in a quasi continuous spectrum of eigenvalues (see chapter 2.2). By expanding the eigenvalues in real and imaginary part $\lambda = \frac{\alpha}{\tau} + i\beta$ and equation (3.1.1) one obtains:

$$\alpha = \frac{1}{2} \ln \left(\frac{B^2}{A^2 + \beta^2} \right). \tag{3.1.8}$$

In figure 3.1.2 the quasi continuous spectrum as well as the leading eigenvalues obtained from eq. (3.1.7) are plotted. One can observe that even for small values of the delay time $\tau = 5$ the quasi continuous spectrum is a good approximation for the exact eigenvalues obtained from eq. (3.1.7). For larger values of τ the distance between the discrete eigenvalues is smaller leading to an increasing number of relevant eigenvalues.
For large delays one can estimate the instability threshold for the steady states by calculating the set of parameters leading to a crossing of the quasi continuous spectrum with the imaginary axis. This point is given by $\alpha = 0$ and $\beta = 0$ because the maximum real part of equation (3.1.8) has a vanishing imaginary part. Depending on whether

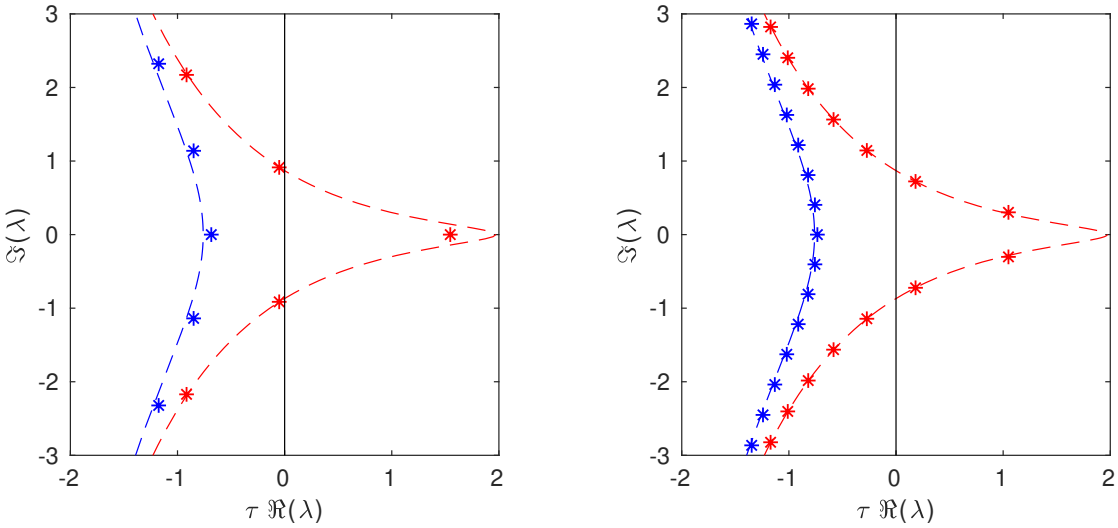

Figure 3.1.2: Eigenvalues λ_s (blue) and λ_u (red) of eq. (3.0.1) corresponding to the steady states $\theta_{s,u}$ for $\tau = 5$ (left) and $\tau = 15$ (right) in the complex plane. The dashed lines show the quasi continuous spectrum (3.1.8) while the stars represent the exact solutions given by the Lambert W functions (3.1.7). Other parameters are $\chi = 1$, $\Delta = 0.5$, $\psi = 0.5$.

the leading discrete eigenvalues are real or a set of complex conjugates the occurring bifurcation is a saddle-node or Hopf bifurcation. Setting α and β to zero in equation (3.1.8) leads to $A^2 = B^2$. The coefficients of the linearized problem given in equations (3.1.3) and (3.1.4) yield the following borders of stability for θ_s and θ_u:

$$\Delta = 1 + \chi \sin(\psi), \tag{3.1.9}$$
$$\Delta = -1 + \chi \sin(\psi) \tag{3.1.10}$$

In addition one obtains:

$$\Delta = \sqrt{1 - 4\chi^2 \cos^2(\psi)} + \chi \sin(\psi) \qquad \forall \psi : 4\chi^2 \cos^2(\psi) < 1 \,\&\, \cos(\psi) < 0 \tag{3.1.11}$$
$$\Delta = -\sqrt{1 - 4\chi^2 \cos^2(\psi)} + \chi \sin(\psi) \qquad \forall \psi : 4\chi^2 \cos^2(\psi) < 1 \,\&\, \cos(\psi) < 0 \tag{3.1.12}$$

for θ_s and:

$$\Delta = \sqrt{1 - 4\chi^2 \cos^2(\psi)} + \chi \sin(\psi) \qquad \forall \psi : 4\chi^2 \cos^2(\psi) < 1 \,\&\, \cos(\psi) > 0 \tag{3.1.13}$$
$$\Delta = -\sqrt{1 - 4\chi^2 \cos^2(\psi)} + \chi \sin(\psi) \qquad \forall \psi : 4\chi^2 \cos^2(\psi) < 1 \,\&\, \cos(\psi) > 0 \tag{3.1.14}$$

for θ_u.
The first two borders equation (3.1.9) and equation (3.1.10) can be identified as the saddle-node bifurcations in equation (3.1.5) and equation (3.1.6).
In figure 3.1.3 the six borders (3.1.9) to (3.1.14) are plotted in the Δ-ψ plane. In the top inset the eigenvalues corresponding to θ_s and θ_u coincide while the leading real eigenvalue crosses the imaginary axis, confirming that the black borders represent a saddle-node bifurcation.
The middle inset shows the eigenvalues at the blue border, here one can observe the quasi continuous spectrum belonging to θ_s crossing the imaginary axis at $\Im(\lambda) = 0$. The

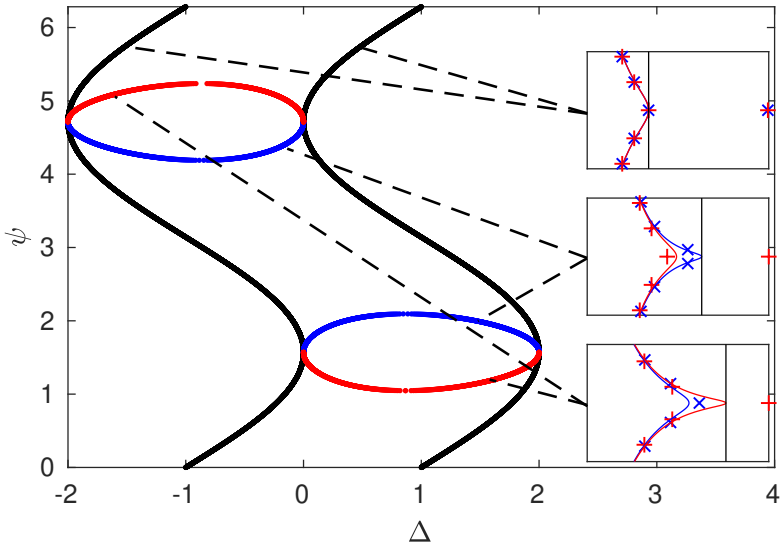

Figure 3.1.3: Borders of stability of the steady states of eq. (3.0.1) calculated in the long delay limit for $\chi = 1$. Borders given by eq. (3.1.9) and (3.1.10) are shown in black, eq. (3.1.11) and (3.1.12) in blue and eq. (3.1.13) and (3.1.14) in red. The insets show the quasi continuous spectrum and the discrete eigenvalues of θ_s in blue and θ_u in red for $\tau = 5$ on these borders.

leading discrete eigenvalues of θ_s in the middle inset are complex conjugates leading to the conclusion that the formerly stable state θ_s becomes Hopf unstable. The eigenvalues on the red border are shown by the bottom inset, where the quasi continuous spectrum belonging to θ_u crosses the imaginary axis. The next eigenvalues of θ_u crossing the imaginary axis in the bottom inset are also complex conjugates but there is a leading real eigenvalue with $\Re(\lambda) > 0$ so the state θ_u is unstable on both sides of the border.

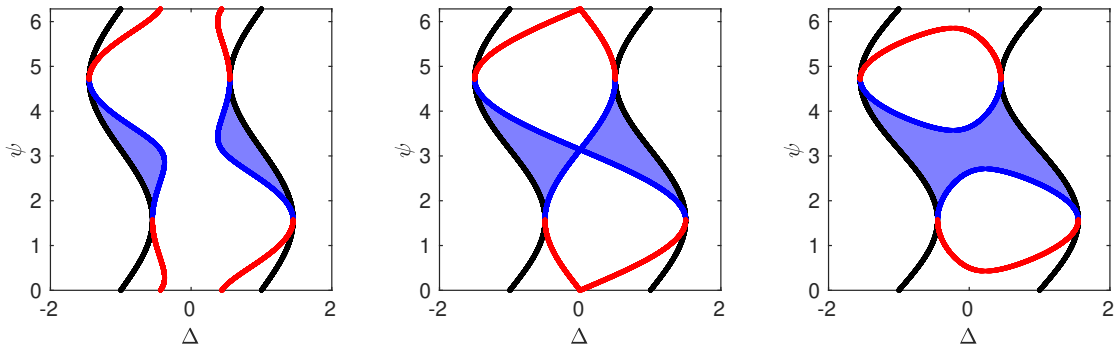

Figure 3.1.4: Region of Hopf instability (blue) in the long delay limit with increasing feedback strength (left $\chi = 0.45$, middle $\chi = 0.5$ right $\chi = 0.55$). The Borders shown in 3.1.3 are included for each value of χ.

The area in which the steady state θ_s is Hopf unstable is especially important because this results in an oscillating background. The change of size and form of this area of Hopf instability in dependence of feedback strength χ was investigated. In figure 3.1.4 the four borders resulting from equation (3.1.9) to (3.1.14) are plotted for different values of χ and the region of instability is colored in blue. For low feedback strengths there are two areas in which the steady state θ_s is Hopf unstable and they are close to the saddle-node bifurcation between $\psi = \pi/2$ and $\psi = 3\pi/2$. With increasing feedback strength these

areas stretch further away from the saddle-node border, until they meet in the center at $\psi = \pi$, $\Delta = 0$ and $\chi = 0.5$. For even bigger feedback strengths of $\chi > 0.5$ the two areas merge into one area of instability.

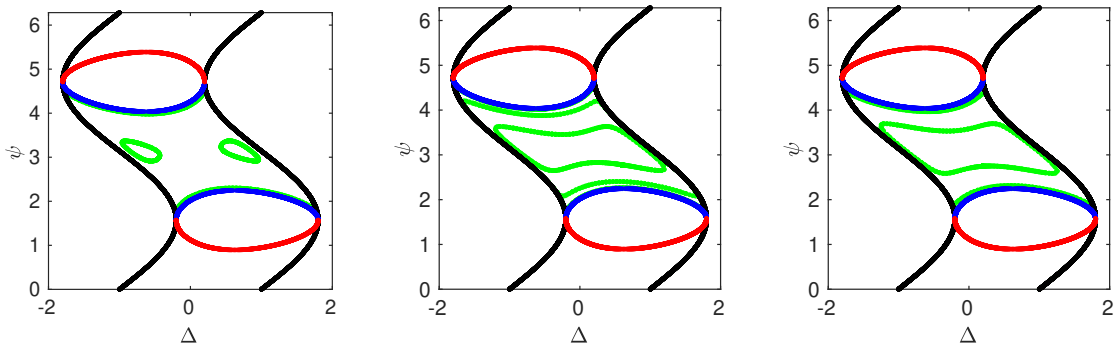

Figure 3.1.5: Borders of Hopf instability (green) obtained from continuation with `dde-biftool` plotted over the stability borders obtained from the long delay limit eq. (3.1.8) for different delay times and $\chi = 0.8$. The delay time increases form $\tau = 10$ (left), $\tau = 20$ (middle) to $\tau = 30$ (right).

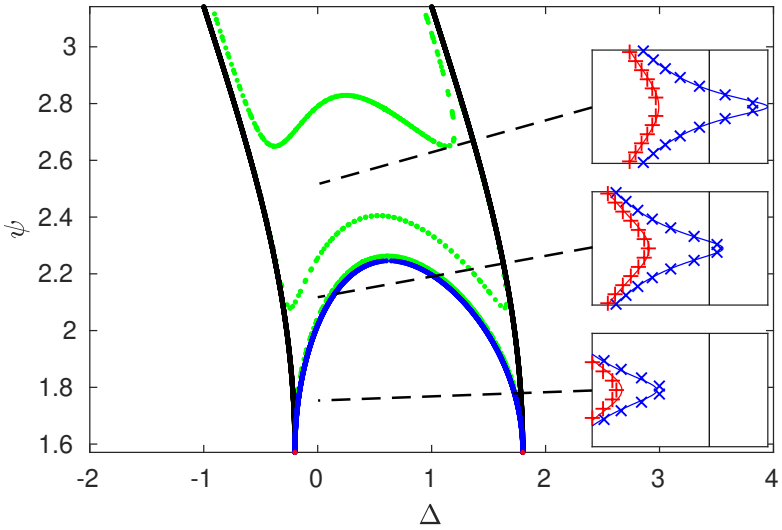

Figure 3.1.6: Borders of Hopf instability (green) obtained from continuation with `dde-biftool` plotted over the stability borders obtained from the long delay limit eq. (3.1.8) for $\tau = 20$ and $\chi = 0.8$. The insets show the eigenvalues of the steady states of eq. (3.0.1), θ_s in blue and θ_u in red, at different points in Δ-ψ-plane with $\tau = 20$.

3.1.1 Continuation of Hopf Instability and Approximation of Discrete Eigenvalues

Using the `dde-biftool` it is possible to follow the state θ_s while varying one Parameter Δ or ψ. If there occurs a Hopf bifurcation it is possible to follow the Hopf point in the Δ-ψ-plane. With this method one obtains several regions of Hopf instability, corresponding to the crossing of the imaginary axis of several pairs of complex conjugate eigenvalues. In figure 3.1.5 the results of the continuation are shown for three different time delays. For each time delay one can observe a Hopf border close to but not exactly at the

border obtained from the long delay limit, corresponding to the crossing of the first pair of complex conjugate eigenvalues with the imaginary axis. For small delay times (left $\tau = 10$) the regions where a second pair of complex conjugate eigenvalues have a positive real part form two separate small ovals centered around $\psi = \pi$.
With increasing delay time the distance between the discrete eigenvalues becomes smaller, while they still follow the quasi continuous spectrum which is independent of the delay time. This leads to a larger region of instability for each pair of complex conjugate eigenvalues crossing the imaginary axis. In the case of figure 3.1.5 the longer delay (middle panel $\tau = 20$) leads to a merging of the two small regions of secondary instability into one large region. For even bigger delay times (right panel $\tau = 30$) the secondary Hopf border approaches the borders of the long delay limit while a third region corresponding to the crossing of the third pair of complex conjugate eigenvalues emerges.
In figure 3.1.6 the eigenvalues of θ_s and θ_u are shown in the three different regions in the middle of figure 3.1.5. The bottom inset corresponds to a point inside of the green circle where the state θ_s is stable. For the middle and top inset the corresponding point lies outside of the region of stability and inside of the region of first (middle inset) and second (top inset) Hopf instability.
In order to get an analytical expression for the Hopf borders shown in figure 3.1.5 the crossing of the discrete eigenvalues with the imaginary axis has to be calculated. The first approach of setting the real part of equation (3.1.7) did not produce a closed form expression so the eigenvalues where approximated. To achieve this the imaginary part was approximated as $\Im(\lambda) = \dfrac{2\pi(n+1/2)}{\tau}$ because the difference in imaginary part between two eigenvalues were expected to be close to $\dfrac{2\pi}{\tau}$ and the leading eigenvalues should be complex conjugates. The real part of the eigenvalues was then calculated by restricting them on the quasi continuous spectrum:

$$\alpha_n = \frac{1}{2} \ln \left(\frac{B^2}{A^2 + \frac{2\pi(n+1/2)}{\tau}} \right). \tag{3.1.15}$$

The roots of this expression can now be calculated resulting in an expression for Δ:

$$\Delta = \pm \sqrt{1 + \frac{4(n+1/2)^2\pi^2}{\tau^2} - 2\chi^2\cos^2(\psi) \pm \frac{\chi\cos(\psi)\sqrt{-16(n+1/2)^2\pi^2 + 4\chi^2\tau^2\cos^2(\psi)}}{\tau}} + \chi\sin(\psi). \tag{3.1.16}$$

Note that these borders vanish if Δ is not real.
By comparing figure 3.1.5 and 3.1.7 one can see that, while the overall shape of the instability regions look similar, there is obviously a mismatch between the results obtained by the continuation and by the approximation of eigenvalues. To illustrate this the approximated eigenvalues are compared to the exact ones in figure 3.1.8. While the approximated eigenvalues are close to the exact ones the distance in imaginary part does not seem to be exactly $\frac{2\pi}{\tau}$ and additionally the exact eigenvalues given by eq. (3.1.7) do not lie exactly on the quasi continuous spectrum. For the eigenvalues of the formerly stable state θ_s this leads to a generally lower real part. By increasing the delay the eigenvalues move closer to each other which, as discussed before, leads to further crossings of complex conjugate pairs of eigenvalues with the imaginary axis and thus further instabilities. In this context of approximated eigenvalues with a generally lower real part

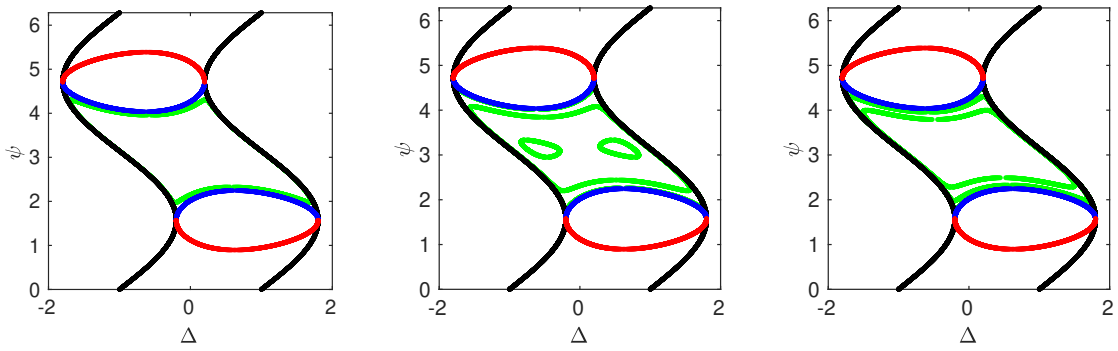

Figure 3.1.7: Borders of Hopf instability obtained from approximation of eigenvalues (eq. (3.1.16)) plotted over the stability borders obtained from the long delay limit (eq. (3.1.8)) for different delay times and $\chi = 0.8$. The delay time increases form $\tau = 10$ (left), $\tau = 20$ (middle) to $\tau = 30$ (right).

this leads to the instabilities occurring for higher values of τ and thus generally smaller instability regions than in the exact case. For example for a delay of $\tau = 10$ the exact borders obtained from continuation (figure 3.1.5) show small regions of secondary Hopf instability while in the approximated case (figure 3.1.7) there is no secondary instability.

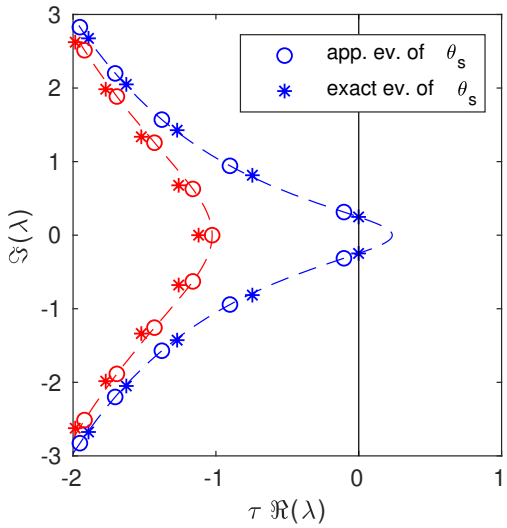

Figure 3.1.8: Comparison of approximated eigenvalues of θ_s (blue) and θ_u (red) obtained from equation (3.1.15) and exact eigenvalues obtained from equation (3.1.7). Calculated for $\tau = 10$, $\Delta = 0$, $\psi = 2.1$ and $\chi = 0.8$

3.2 Periodic Orbits / Localised States

In the region surrounding the saddle-node bifurcation the system is excitable. A small perturbation from the stable state θ_s reduces exponentially because the system is linearly stable. If however the system is close to the saddle-node bifurcation the states θ_s and θ_u are close as shown in figure 3.1.1. In this case a relatively small perturbation can excite the system beyond the linearly unstable state θ_u leading to a trajectory towards $\theta_s + 2\pi$ instead of relaxing back to θ_s. This means a small perturbation of a stable state can lead to a large orbit in phase space.
If we now introduce time delay into this excitable system one excitation at the time $t-\tau$ can lead to another excitation at time t resulting in a periodic repetition of excitations with an approximate period of the delay time τ. This is demonstrated in figure 3.2.1 where the results of a numeric integration of $\theta(t)$, performed with a starting condition that approximates an excited orbit, are shown.

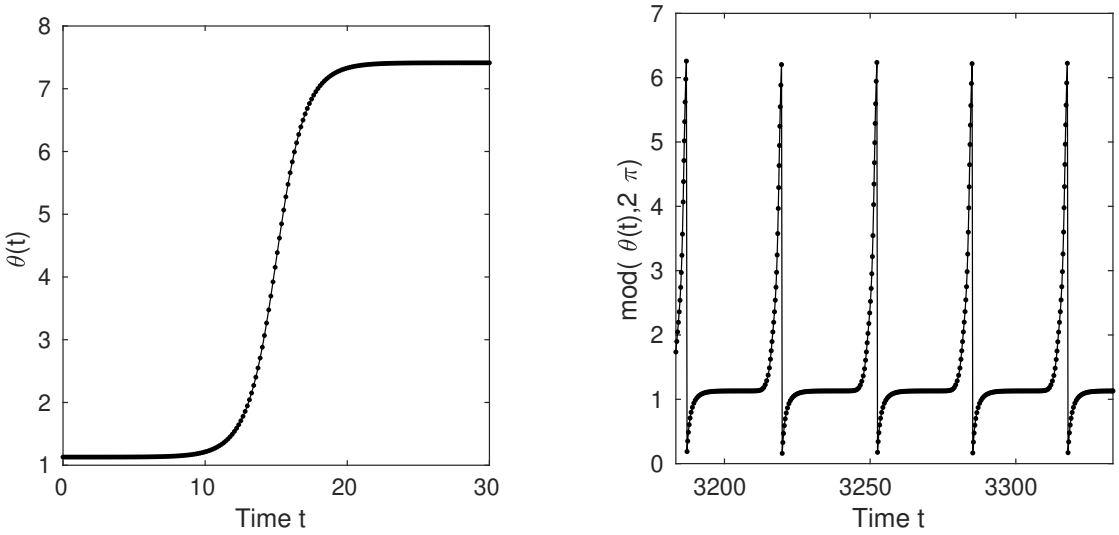

Figure 3.2.1: Starting profile of the time integration (left) and resulting time trace of $\theta(t)$ (right). Calculations where made for feedback strength $\chi = 0.3$, detuning $\Delta = 1.2$, delay phase $\psi = 1.4$ and delay time $\tau = 30$.

To further investigate the excited orbits with the help of `dde-biftool` they are implemented as periodic orbits from θ_s to $\theta_s + 2\pi$ with period T. Instead of using the approximation for the excited orbit, that was used as a starting profile for the integration in figure 3.2.1, the profile was extracted from the integrated time trace. The periodic solutions where then continued in Δ and T while adjusting the profiles of $\theta(t)$. It is also possible to determine the stability of a periodic solution by calculating the spectrum of Floquet multipliers of the corresponding poincare map via `dde-biftool`. The resulting branch of solutions is shown in figure 3.2.2. One can observe two stable regions, one having a period slightly above $\tau = 30$ and the other one having a period slightly above $\frac{\tau}{2} = 15$.
To achieve a better visualisation of the periodic solutions the topological charge Q corresponding to the number of 2π-phase differences per time delay τ is introduced:

$$Q = \frac{\tau}{2\pi(T_1 - T_0)} \int_{T_0}^{T_1} \frac{\mathrm{d}\theta}{\mathrm{d}t} \mathrm{d}t. \tag{3.2.1}$$

For the profiles used in `dde-biftool`, equation (3.2.1) simplifies to $Q = \frac{\tau}{T}$, because all profiles have a total phase difference of 2π. For longer time traces resulting from numeric integrations one obtains $Q = \frac{\tau}{T_1 - T_0} \frac{\theta(T_1) - \theta(T_0)}{2\pi}$.

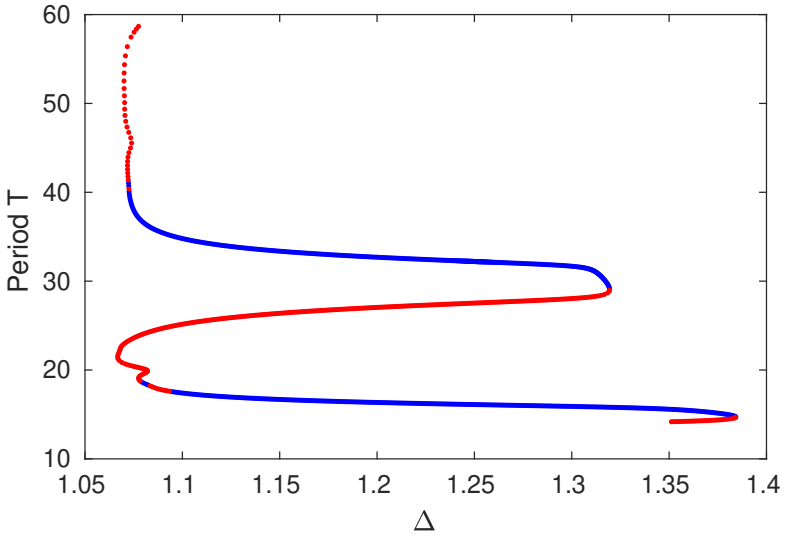

Figure 3.2.2: Continuation of the periodic solutions in detuning Δ and period T for $\chi = 0.3$, $\psi = 1.4$ and $\tau = 30$. Blue parts represent stable orbits while red parts represent unstable orbits.

For the parameters used in the calculations shown in figure 3.2.2 ($\psi = 1.4$, $\chi = 0.3$) the steady state θ_s vanishes at $\Delta = 1.296$ but the continuation clearly shows stable periodic solutions for values of $\Delta > 1.296$. To investigate this region further, a numeric integration was performed starting with the state θ_s at $\Delta = 1.25$. After integrating for a time long enough to ensure stability of the result the parameter Δ was changed and the next step of integration was performed starting with the result of the former integration. First Δ was increased up to 1.35 which lies outside of the range of existence of θ_s. After reaching $\Delta = 1.35$ the process was continued in the other direction till $\Delta = 1$. For each step the topological charge Q was calculated using equation (3.2.1). In figure 3.2.3 the topological charge Q is shown for the results of the time integration and the continuation.
One can observe that the system starts and stays in the state θ_s which has a topological charge of 0 until around $\Delta = 1.296$ the system jumps to the stable branch with $Q \approx 1$. At the point where the stable periodic solution with $Q \approx 1$ disappears in a saddle-node bifurcation the system jumps to the stable solution with $Q \approx 2$ which is stable up to values of $\Delta > 1.35$.
In the reverse direction where Δ is decreased from $\Delta = 1.35$ to $\Delta = 1$ one can observe a hysteresis because there is a region ranging from $\Delta \approx 1.1$ to $\Delta \approx 1.3$ where all three solutions with $Q = 0$, $Q \approx 1$ and $Q \approx 2$ are stable. After reaching $\Delta \approx 1.1$ the system falls back to the solution with $Q \approx 1$ which also gets unstable for $\Delta \approx 1.075$ resulting in the system falling back to θ_s with $Q = 0$.

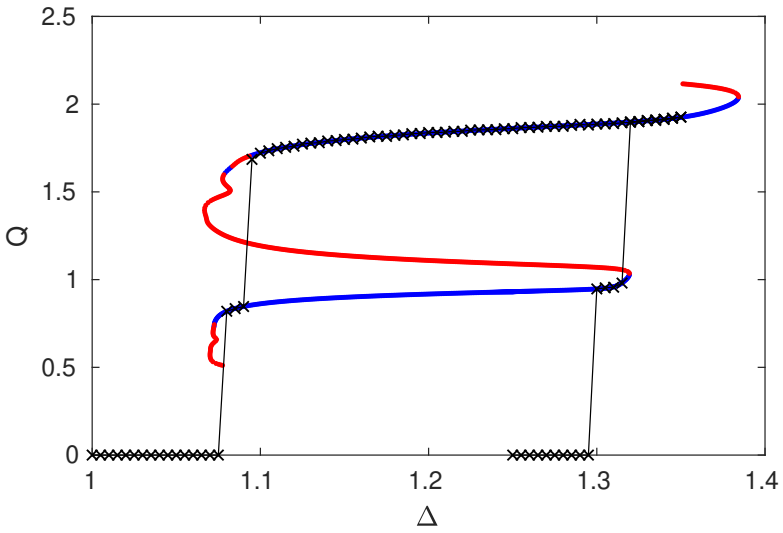

Figure 3.2.3: Bifurcation diagram of periodic solutions obtained from continuation with dde-biftool (blue stable, red unstable) and time integration (black). $\psi = 1.4$, $\chi = 0.3$ and $\tau = 30$.

3.2.1 Antikinks

Going back to figure 3.1.1 it is not only possible to excite a trajectory from θ_s to $\theta_s + 2\pi$ but also from θ_s to $\theta_s - 2\pi$. This requires the system to be in the vicinity of the left saddle-node bifurcation towards negative values of the detuning. In figure 3.2.4 the same calculations shown in figure 3.2.3 where made for trajectories with a negative phase difference, which from now on will be called antikinks, whereas those solutions with a positive phase difference will be called kinks. The results for the antikinks match the ones of the kink solution where Q, Δ and ψ are inverted. This can be directly derived via eq. (3.0.1) by substituting Δ, θ and ψ with $\Delta' = -\Delta$, $\theta' = -\theta$ and $\psi' = -\psi$ resulting in the same system for θ'.

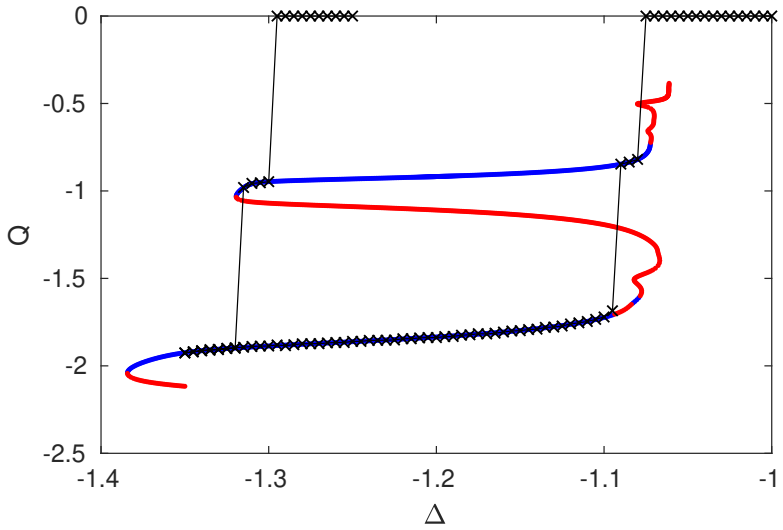

Figure 3.2.4: Bifurcation diagram of antikink solutions obtained from continuation with dde-biftool (blue stable, red unstable) and time integration (black). $\psi = -1.4$, $\chi = 0.3$ and $\tau = 30$.

Because of this an investigation of the behavior of antikink solutions on their own is not necessary as long as the dynamics of the corresponding kink solution is known. Nonetheless the existence of antikinks has a interesting aspect which is the possible coexistence and interaction of kinks and antikinks.

To investigate the coexistence of kinks and antikinks the continuation of the periodic solutions in Δ was performed for three different feedback strengths and for kinks and antikinks respectively. In figure 3.2.5 the results for $\chi = 0.8$, $\chi = 1.5$ and $\chi = 3$ are shown. One can observe that an increase in feedback strength generally leads to a larger region of stability for the kink and antikink solutions. For $\chi = 3$ there is a a coexistence of the kink and antikink soulutions up to a topotlogical charge of $|Q| = 2$ spanning from $\Delta \approx -0.7$ to $\Delta \approx 0.7$.

The unstable branches of the bifurcation diagram in figure 3.2.5 show a series of loops between the stable branches. Those loops increase in size and density with increasing feedback strength. In the case of high feedback strength ($\chi = 3$) the looping behavior was too much to continue a single branch from the solution with $Q = 1$ to a solution with $Q = 2$. Instead a separate branch was calculated with a starting condition extracted from another time integration. The resulting branches should be connected as it is the case for $\chi = 0.8$ and $\chi = 1.5$.

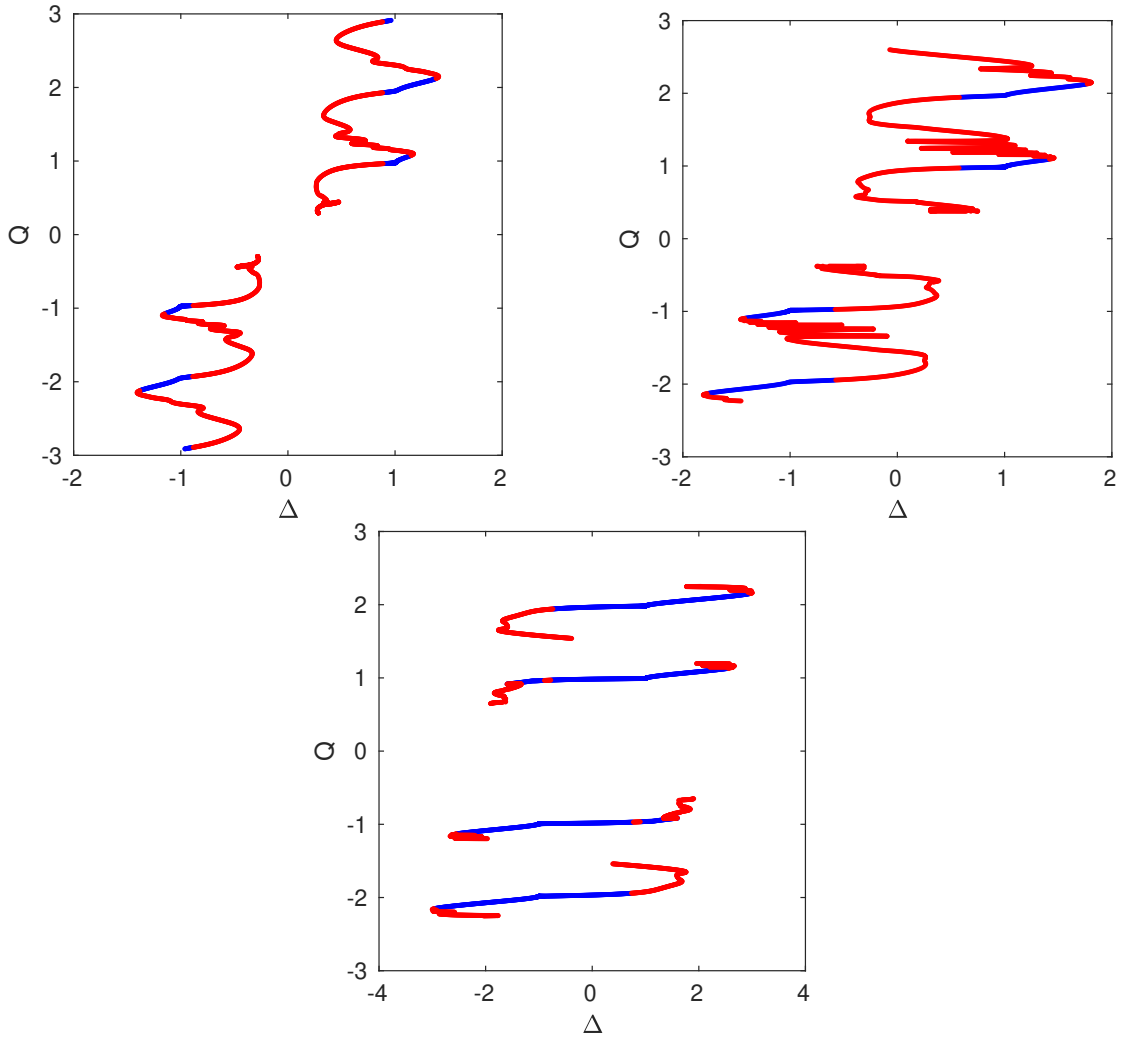

Figure 3.2.5: Bifurcation diagram of kink and antikink solutions for $\psi = 0$, $\tau = 30$, $\chi = 0.8$ (top left), $\chi = 1,5$ (top right) and $\chi = 3$ (bottom). Stable solutions are shown in blue, while unstable ones are shown in red.

Another interesting question arising in this context is whether or not the kink and antikink branches are connected with each other or with the steady state θ_s which has a topological charge of $Q = 0$.

3.2.2 Continuation of Bifurcations in Δ-ψ Plane

Using the `dde-biftool psol` extension it is posssible to track the point at which a branch of periodic solutions loses stability. In order to achieve this the Floquet multipliers determining the stability of the periodic solution need to be calculated. Depending on where one or several of these Floquet multipliers leave the unit circle, different bifurcations can take place. In particular a crossing of a Floquet multiplier at $\mu = 1$ leads to a fold bifurcation while $\mu = -1$ leads to a period doubling bifurcation and a crossing of a pair of complex conjugate eigenvalues leads to a torus bifurcation [21]. Each of these bifurcation types can be continued by `dde-biftool` in the Δ-ψ plane. At this point it is important to note that dde-biftool treats a period doubling bifurcation as special case of torus bifurcation [27].

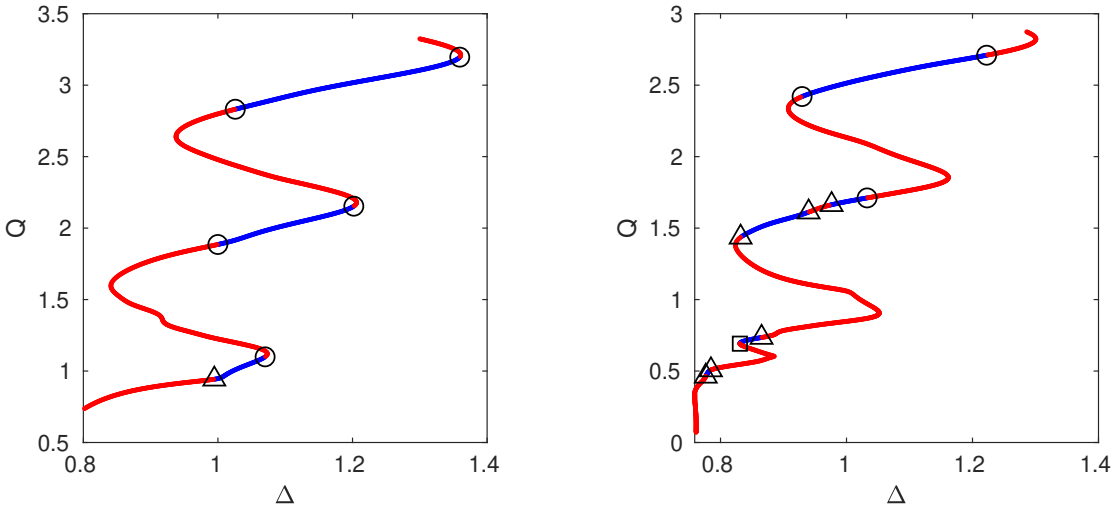

Figure 3.2.6: Bifurcation diagram of kink solutions for $\chi = 0.3$, $\tau = 30$ and $\psi = 0$ (left) and $\psi = \pi$ (right). The different instabilities are marked with squares for fold bifurcations, triangles for period doubling bifurcations and circles for torus bifurcations. Stable solutions are shown in blue, while unstable ones are shown in red.

As shown in fig. 3.2.6 all three types of bifurcations are involved in the stability of periodic orbits. In figure 3.2.7 the Floquet multipliers corresponding to each instability type, occurring in the two branches at $\psi = 0$ and $\psi = \pi$, are displayed. There is always one Floquet multiplier with exactly $\mu = 1$ that is displayed as stable (green) in the left and right panel but as unstable in the middle panel, due to numerical inaccuracy. The corresponding mode is simply a time shift, which will neither grow nor reduce over time meaning $\theta(t - t_{\text{shift}})$ is as good as a solution as $\theta(t)$ since the system does not explicitly depend on the time t.
The continuation of the fold bifurcation is shown in figure 3.2.8. In addition to the borders of stability in the Δ-ψ plane the topological charge Q was calculated for the profiles involved in the bifurcation and plotted in dependence of Δ and ψ, respectively. In figure 3.2.8 (left) the saddle-node and Hopf bifurcations of the steady state θ_s are included as a reference.
As can be seen in bifurcation diagrams of the periodic solution (figure 3.2.6) the solutions with higher topological charge Q have folds that typically reach farther into the region where no steady states exist ($\Delta > 1+\chi\sin(\psi)$). This can also be seen in the continuation of the fold bifurcations, because there are multiple fold bifurcations when moving away

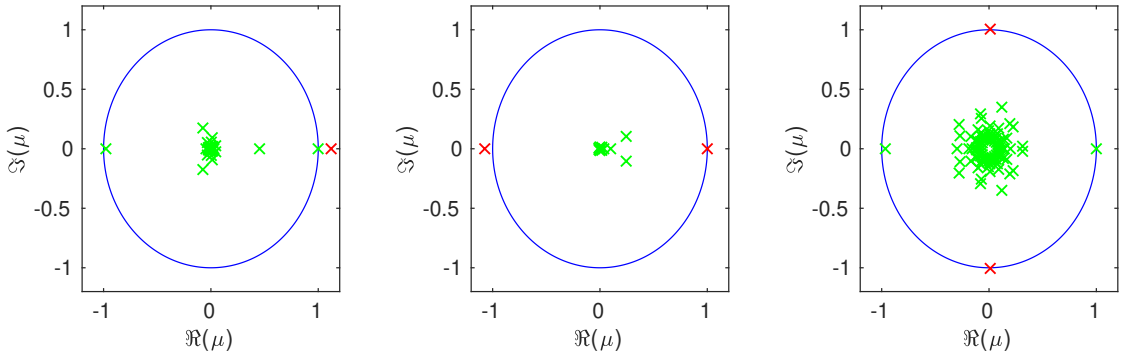

Figure 3.2.7: Spectrum of Floquet multipliers for the three bifurcation types: fold bifurcations on the left, period doubling bifurcations in the middle and torus bifurcations on the right. The blue circle represents the unit circle. There is always one Floquet multiplier with $\mu = 1$ that corresponds to the translation invariance.

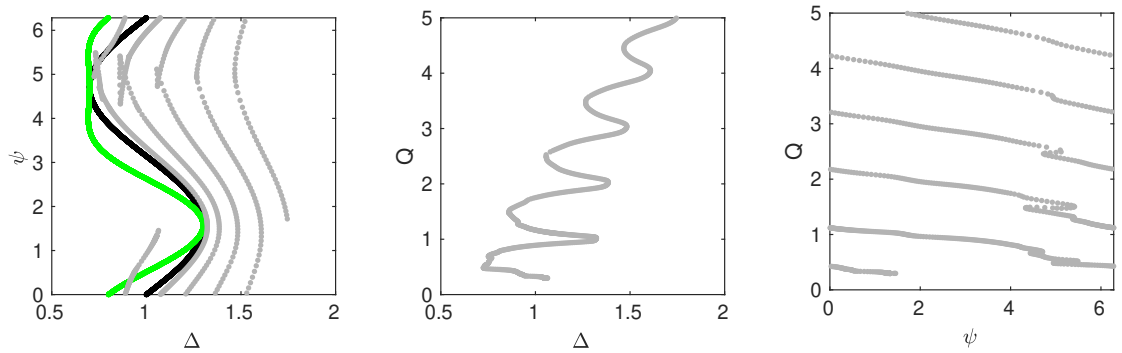

Figure 3.2.8: Continuation of fold of periodic solutions for $\chi = 0.3$ and $\tau = 30$. Borders of stability in Δ-ψ plane (left) and dependence of Q on Δ (middle) and ψ (right) are presented. The left panel includes the fold and Hopf bifurcations of the steady state in black and green.

from the region of steady states in the left of figure 3.2.8. However, something that is not apparent from the bifurcation diagrams of periodic solutions, is that those fold bifurcations seem to be connected. This can clearly be seen in the right panel of figure 3.2.8 where the topological charge Q is plotted against the feedback phase ψ which is 2π periodic. This implies that the periodic solutions witch topological charge Q and $Q+1$ not only lie on the same branch, but there can possibly be one stable region connecting the two when taking the additional parameter ψ into account.

In figure 3.2.9 the period doubling bifurcations are displayed in the same manner as the fold bifurcations in figure 3.2.8. In the left panel one can see that those bifurcations seem to be in similar regions as the Hopf instabilities of the steady states. They also seem to only be involved with solutions of topological charge $Q \leq 1$. The results of the continuation do not show closed bounded regions as can be seen in the middle and right panel of figure 3.2.9 which indicates that the results are incomplete. There were in fact several points in this continuation where the process stopped and a specific point had to be skipped manually.

In contrast the continuation of the torus bifurcations went much more smoothly and without halting. In figure 3.2.10 the results are also shown in the same way. On the first

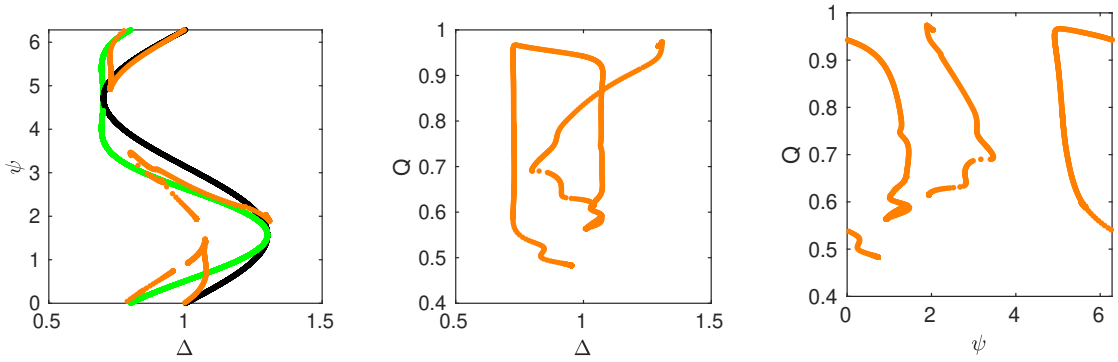

Figure 3.2.9: Continuation of period doubling of periodic solutions for $\chi = 0.3$ and $\tau = 30$. Borders of stability in Δ-ψ plane (left) and dependence of Q on Δ (middle) and ψ (right) are presented. The left panel includes the fold and Hopf bifurcations of the steady state in black and green.

glance the projection on the Δ-ψ plane looks similar to the period doubling bifurcations. The regions of instability lie in the vicinity of the background Hopf instability but reach further in to the region of no steady states. In the middle and right panel one can see that the regions of instability lie between $Q = 1$ and $Q = 2$ as well as $Q = 2$ and $Q = 3$ but do not span over whole numbers of Q. Unlike the period doubling instabilities the torus instabilities form closed regions which can be seen best in the right part of figure 3.2.10. Here one can also observe the upper regions of instability with $2 < Q < 3$ having a generally similar shape as the lower ones with $1 < Q < 2$.

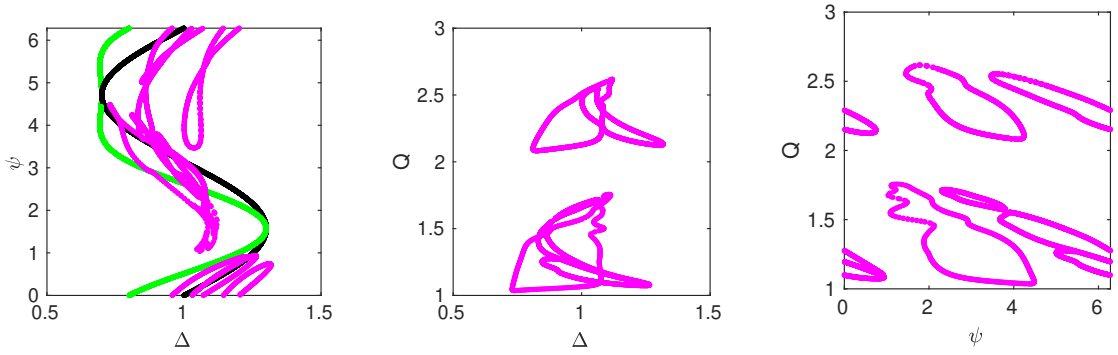

Figure 3.2.10: Continuation of torus bifurcation of periodic solutions for $\chi = 0.3$ and $\tau = 30$. Borders of stability in Δ-ψ plane (left) and dependence of Q on Δ (middle) and ψ (right) are presented. The left panel includes the fold and Hopf bifurcations of the steady state in black and green.

A more intuitive way of displaying these instabilities is a three dimensional representation with Δ, ψ and Q on the axis instead of just two dimensional projections. For this, several branches of periodic solutions where calculated for equidistant values of ψ. The resulting point cloud was then interpolated into a two dimensional surface of periodic solutions. There is certainly a loss of accuracy in this interpolation but the resulting surface is only used for illustrative purposes. In figure 3.2.11 one perspective of this surface is plotted in the three dimensional representation, as well as the background instabilities of the steady state at $Q = 0$ and the three types of instabilities for the periodic solutions. The overall structure is hard to display in a two dimensional projection. A video of the full 3D structure can be found at: https://uni-muenster.sciebo.de/s/Dv5z4lF25Scs0kM.

Here one can clearly see that the stable regions of periodic solutions form one connected surface that increase in Q by 1 if one increases ϕ gradually by 2π. This band of stable solutions is sometimes interrupted by the torus or period doubling bifurcations leading to unstable regions inside the stable surface. Since all branches of periodic solutions that were continued in Δ for a specific value of ψ represent a cut of this surface, those regions of instability lead to a splitting of the stable regions as can be seen in the right panel of figure 3.2.6.

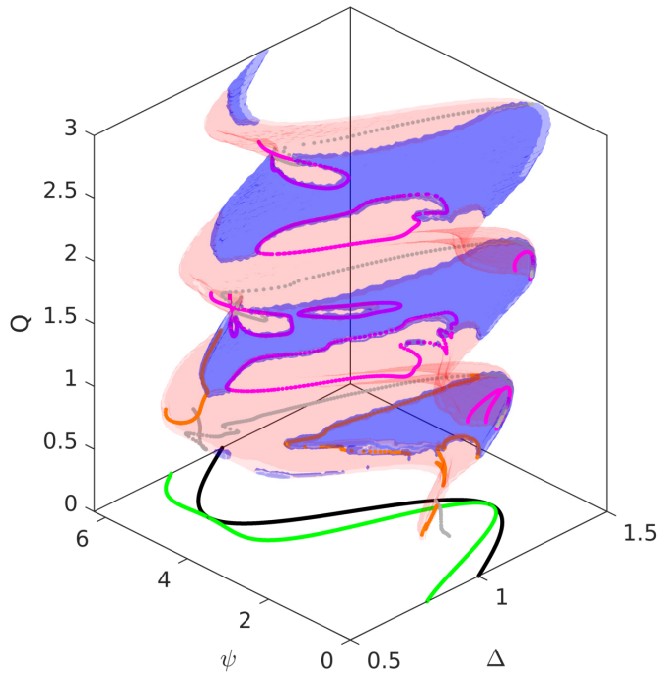

Figure 3.2.11: 3D bifurcation diagram of periodic solutions in Δ and ψ. Blue and red regions show stable and unstable periodic solutions while the fold bifurcations are shown in grey, the torus bifurcations in magenta and the period doubling bifurcations in orange. The long delay instabilities of the steady state have been added in black and green at $Q = 0$ as a reference.

One can also see that the resulting 3D representation is not complete, since not all borders between the blue (stable) and red (unstable) surface are marked with results of the continuation of an instability. In order to find the borders of stability only the bifurcation points of the two branches shown in figure 3.2.6 were used as starting points for the continuation. Additionally, one could extend the surface of solutions to higher numbers of $Q > 3$ where even more torus bifurcations with similar shape are expected. Another interesting area that is left out by this representation are the solutions with low values of Q which correspond to a period $T \gg \tau$ that is far greater than the delay. While this region could shed light upon the connection between steady states and periodic solutions it was left out due to the high computation time of solutions with high periods. This matter is investigated further in section 3.2.4.

Finally we can conclude that, even if not complete, we were able to draw a picture of the existence and stability of periodic solutions in the delayed Adler equation (3.0.1).

Furthermore we revealed a high level of complexity regarding those periodic solutions especially in the region of $\psi \in [\pi/2, 3\pi/2]$.

3.2.3 Properties of Localized States

Up to now the solutions of repetitive excitation have been regarded as periodic solutions. However if the excitation itself happens fast in comparison to the delay time τ the system could be described as being in the steady state θ_s for most of the time. In this case one could add a second excitation that would also repeat itself after approximately the delay time τ without interfering with the repetition of the first excitation. In this case one repeating excitation can be described as a temporal localised state (LS). Although periodic, one kink would only occupy a small time of each period.
In order to investigate the localised nature of these solutions it is important to take a look at the temporal width of each kink and its dependence on the system parameters. For this the most important parameters seem to be the delay τ itself, because in the context of localised states it relates to the domain size the LSs exist in. Further important parameter is the feedback strength χ which is comparable to the scaling of an external forcing if one only considers one period.

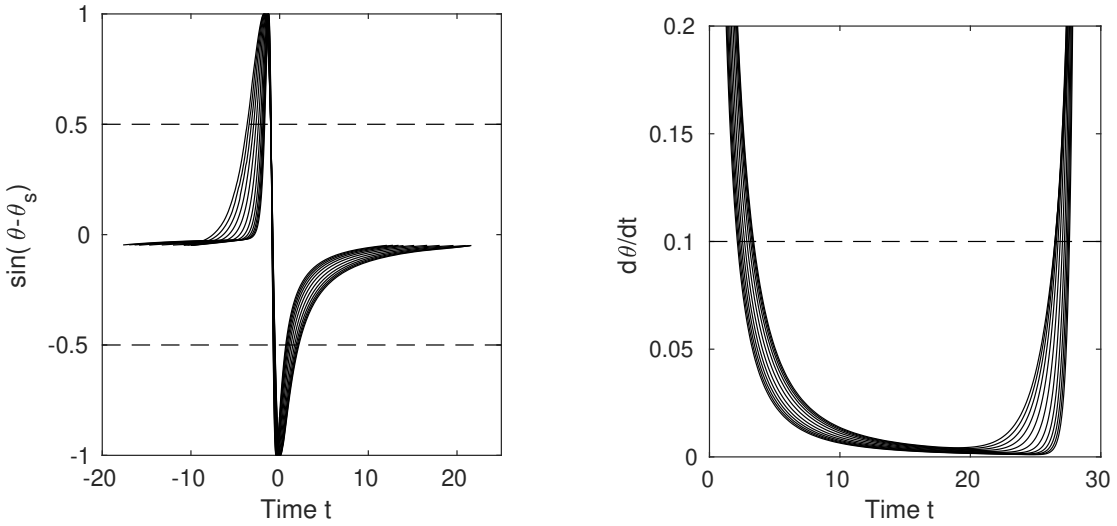

Figure 3.2.12: Visualisation of the two definitions of width. The left panel shows $\sin(\theta(t) - \theta_s)$ with thresholds 0.5 and -0.5, while the right panel shows $\mathrm{d}\theta/\mathrm{d}t$ with threshold 0.1. Both panels show the same set of periodic solutions for different feedback strengths χ.

To investigate the width of periodic solution we need to define a measure for it. In other examples of pulses like gaussian pulses the width is often defined as the full width at half maximum (FWHM) or similar definitions. In our case this definition does not apply, because the periodic solutions do not converge to the same value on the left and right end. We can either force the LS to converge to zero in both directions by calculating $\sin(\theta(t)-\theta_s)$ or take a different approach of defining the width using the derivative of $\theta(t)$. In fig. 3.2.12 the profiles of several LS were calculated for different feedback strengths χ. In the left panel the first definition of the width as the time between $\sin(\theta-\theta_s) = 0.5$ and $\sin(\theta - \theta_s) = -0.5$ is depicted. The right panel shows the derivative of $\theta(t)$ as well as a threshold of $\mathrm{d}\theta(t)/\mathrm{d}t = 0.1$. The system is assumed to be approximately in the steady state θ_s if the derivative is lower than the given threshold, making the time

where $\mathrm{d}\theta(t)/\mathrm{d}t > 0.1$ the width of the LS. To distinguish between the two definitions the first definition will from now on be called definition W_+ and the second one $W_\circ$.
In [11], the delayed Adler equation (3.0.1) was approximated by multiple time scale analysis, resulting in a partial differential equation without delay:

$$\frac{\partial\theta}{\partial t} = \sin(\bar{\theta}) - \sin(\theta) + \frac{\partial^2\theta}{\partial x^2} + \tan(\psi)\left(\frac{\partial\theta}{\partial x}\right)^2. \tag{3.2.2}$$

One can identify this equation as a overdamped Sine-Gordon equation. It was found that this equation is able to reproduce the existence of localised states as homoclinic orbits of the form [30]

$$\theta(x) = 4\arctan(e^x)$$

that evolve in the slow timescale t. In the derivation of this equation a drift velocity $v = (\chi\cos(\psi))^{-1}$ was compensated and the fast timescale, representing the spatial variable x, had to be rescaled by $(\sqrt{2\chi\cos(\psi)})^{-1}$. This can be seen as an estimate for the dependency of width and the deviation $T - \tau$ on the feedback strength χ.

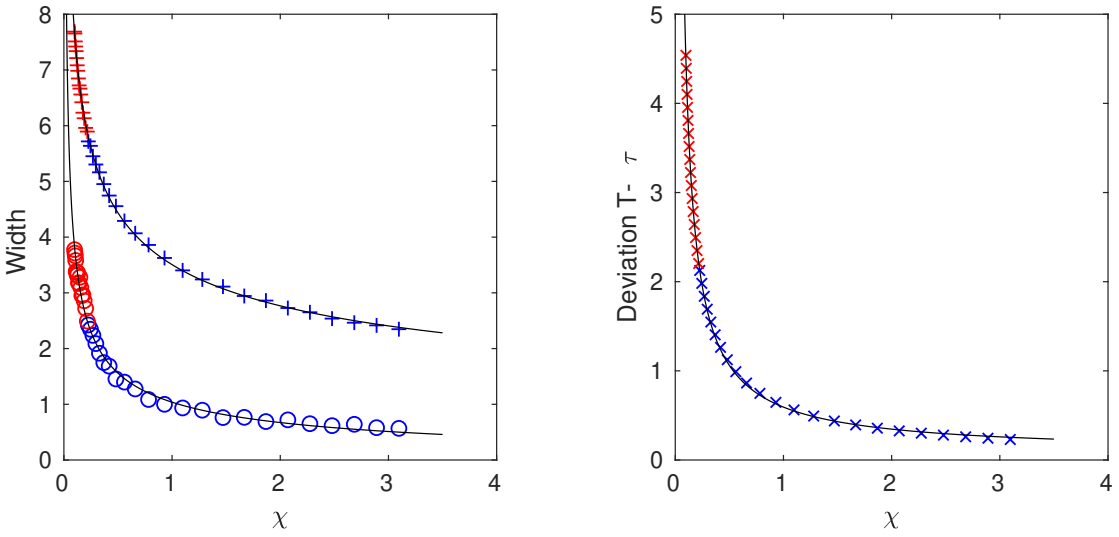

Figure 3.2.13: Branch of periodic solutions with feedback strength χ as a control parameter. Left panel shows the width were the two definitions are marked with circles for $W_\circ$ and crosses denoting W_+. Points marked in blue are stable, while red markers are unstable solutions and the black line shows the result of a fitted power function. The dependence of the deviation $T - \tau$ on the feedback strength is shown in the right panel. Other parameters: $\Delta = 1$, $\psi = 0$ and $\tau = 30$.

Figure 3.2.13 shows a branch of periodic solutions that was calculated at $\Delta = 1$, $\psi = 0$ and $\tau = 30$ with the feedback strength χ as a free parameter. For the resulting profiles both measures of width were calculated and are shown in the left panel. The right panel shows the deviation between the delay τ and the period T of the periodic solution. In both panels stable solutions are marked in blue while unstable ones are shown in red. A power function of the form $A\chi^B + C$ was fitted to both definitions of width and the deviation respectively:

$$
\begin{aligned}
W_+ =& 3.6\chi^{-0.33} - 0.11, \\
W_\circ =& 1.2\chi^{-0.51} - 0.19, \\
T - \tau =& 0.52\chi^{-0.92} + 0.069.
\end{aligned}
$$

Comparing the results with the expected scaling the definition $W_\circ$ and the deviation $T-\tau$ match rather good with exponents $\chi^{-0.51}$ and $\chi^{-0.92}$ in contrast to the expected $\chi^{-0.5}$ and χ^{-1} from the overdamped Sine-Gordon equation (3.2.2). However the definition W_+ seems to produce a cube root dependency instead of a square root.

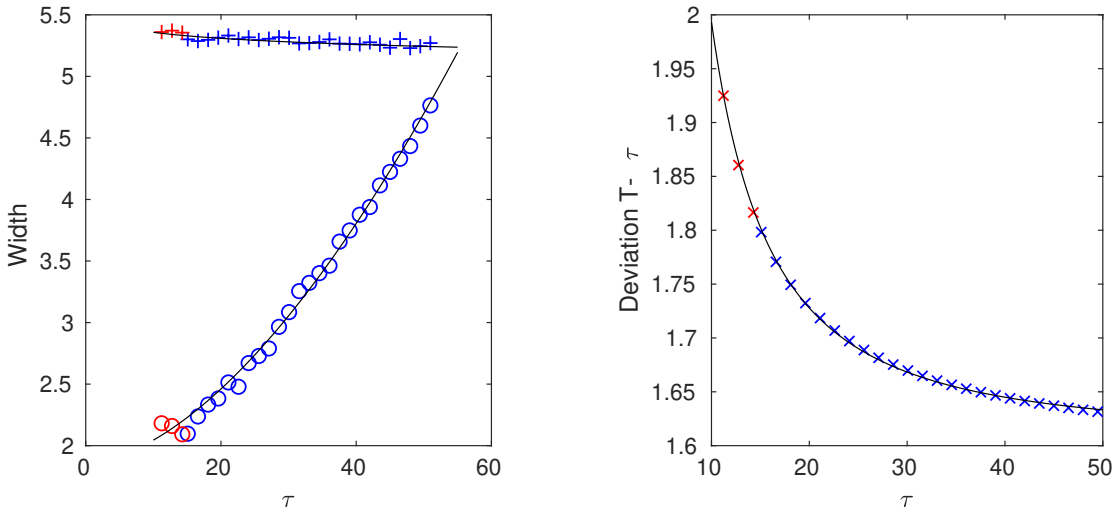

Figure 3.2.14: Branch of periodic solutions with the delay τ as a control parameter. Left panel shows the width were the two definitions are marked with circles for $W_\circ$ and crosses denoting W_+. Points marked in blue are stable, while red markers are unstable solutions and the black line shows the result of a fitted power function. The dependence of the deviation $T - \tau$ on the feedback strength is shown in the right panel. Other parameters: $\Delta = 1$, $\psi = 0$ and $\chi = 0.3$.

The dependence of the width on delay τ is shown in fig. 3.2.14 in the same manner as in fig. 3.2.13. The branch was calculated for $\Delta = 1$, $\psi = 0$ and $\chi = 0.3$. The resulting fitted functions are:

$$
\begin{aligned}
W_+ =& -5\tau^{0.014} + 10, \\
W_\circ =& 0.0038\tau^{1.7} + 1.9, \\
T - \tau =& 18\tau^{-1.7} + 1.6.
\end{aligned}
$$

If the periodic solutions can be described as localised states, they should not depend on the length of the time delay, because in this context it resembles something similar to the domain size in a spatial system. Looking at the results of the left panel in fig. 3.2.14 we can see that, depending on the definition of width, the width either depends strongly ($\tau^{1.7}$) in the case of $W_\circ$ or only slightly ($\tau^{0.014}$) for W_+ on the delay.

While both definitions are a valid descriptions of width, W_+ is better suited in the context of localised states and will therefore be used in the following sections of this thesis. Nonetheless, one has to be careful when describing these periodic solutions as localised states, because their width can be in the range of the delay τ itself. In this case the system could not be described as being approximately in the steady state θ_s for the most time. The effects of the residual dynamics in to, or out of, the steady state outside of the width W_+ will be discussed in section 3.3 where the interaction of multiple LSs through their tails is investigated.

3.2.4 Connection with Steady State / Emergence

An interesting kind of periodic solution are those, whose period T is much greater than the delay τ, because those solutions have a small value of Q and therefore approach the steady state with $Q = 0$. In fig. 3.2.11 these solutions were left out due to computation time. In the previous section 3.2.3 we already observed a growing deviation between the period T and the delay τ for small values of χ and τ. In this section we will investigate those solutions with low topological charge Q to learn more about the connection between the branch of periodic solutions and the steady state.

One possible connection involves the Hopf instability of the steady state θ_s, which was investigated in section 3.1. In fig. 3.1.5 we showed that the regions of Hopf instability grow with increasing delay τ. We could therefore prepare the system in a point with stable steady state θ_s for small delays and make it Hopf unstable by increasing the delay time. With a further increase in delay the Hopf instability could grow and excite the system leading to a periodic solution of excitations.

Since a Hopf instability leads to periodic oscillations close to the threshold and due to the frequent use of the term *periodic solutions* for repetitive excitations we will constrict the use of the term *periodic solutions* to those solutions exhibiting repetitive excitations and refer to the oscillations arising from Hopf instabilities as *oscillations* in that follows.

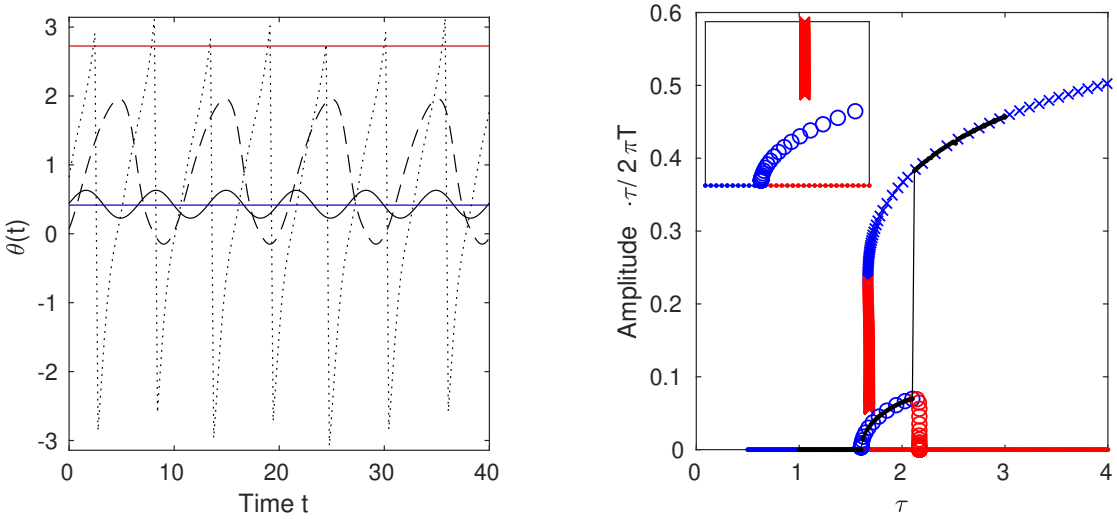

Figure 3.2.15: Trajectories of $\theta(t)$ obtained for increasing delay time τ starting with the steady state θ_s in the Hopf unstable regime ($\chi = 1$, $\psi = 2.84$, $\Delta = 0.7$). The left panel shows three snapshots of the integration from $\tau = 1$ to $\tau = 3$ with $\tau = 1.62$ (black line), $\tau = 2.1$ (dashed line) and $\tau = 2.12$ (dotted line) as well as the steady states θ_s (blue line) and θ_u (red line). On the right a continuation was performed for the three involved states: the steady state (dots) the oscillating state (○) and the periodic state (x), while stable solutions are marked in blue and unstable ones in red. The black line shows the corresponding values of the direct numerical integration. The inset shows the same diagram zoomed in on the lower end of the branch of periodic solutions.

Figure 3.2.15 shows the results of a direct numerical simulation (DNS) that starts with the steady state θ_s and gradually increases in delay τ while making sure to integrate long enough to let the system reach a stable solution in each step. The left panel shows

three profiles of the integration. The first profile at $\tau = 1.62$ (solid black line) is the first one to show oscillations around the steady state (blue), the second profile is the last profile to show oscillations at $\tau = 2.1$ (black dashed line) and the profile at $\tau = 2.12$ (black dotted line) is the first profile showing periodic solutions.
Each of these states, the system is in during the integration, was used as a starting point for a continuation in τ to show how they relate. In order to compare the branch of periodic solutions and the oscillations in a single bifurcation diagram we have to adjust our measure Q. With the definition given in (3.2.1) both the steady state and the oscillations would have a topological charge of 0. While this accurately represents the number of 2π phase flips that happen in a delay time τ, since the oscillation does not lead to a total phase change in one period, we want to observe the transition between those states. For this reason a different measure was used to display the different branches in the right panel of fig. 3.2.15:

$$\frac{\text{Amplitude} \cdot \tau}{2\pi T}. \tag{3.2.3}$$

When defining the amplitude of the periodic solutions as 2π this coincides with the formerly used topological charge Q, while having a nonzero value for oscillations.
In the right panel of fig 3.2.15 the three branches of solutions are displayed with the given measure at the y-axis. One can clearly see the stable oscillating branch (blue $\circ$) emerging from the Hopf bifurcation point of the steady state at $\tau \approx 1.6$. The branch of periodic solutions (x), however, does not seem to emerge out of the point where the oscillation looses stability and is not connected to the branch of oscillations.
The problem could lie in the definition of the periodic solutions. While the steady state and the oscillations do not have a total phase change in one period the periodic solutions always have a phase difference of 2π. However, the periodic solutions still reach values of Q that are much lower than one and seem to approach $Q = 0$ for certain values of τ. This is only possible if the period T of the periodic solutions diverge indicating a global bifurcation connecting the periodic solution with the steady state. The inset of the right panel in fig. 3.2.15 shows the lower end of the branch of periodic solutions. Here one can see the unstable part of the branch of periodic solutions approaching the unstable part of the branch of steady states, however due to the divergence of the period T it is not possible to directly observe the connection between those branches in the continuation.
Since the Adler equation without delay (2.1.1) is sometimes considered to be the normal form of the global saddle-node infinite period bifurcation (SNIPER) [31], we expect the global bifurcation, connecting steady state and periodic solution, in the case of the delayed Adler equation, to be a SNIPER as well. This bifurcation leads to the emergence or destruction of periodic solutions through a saddle-node bifurcation of steady states. As the system approaches the SNIPER the trajectory slows down significantly at one point of the periodic solution, until a steady state appears at the bifurcation point and the period diverges. Beyond the bifurcation point the steady state splits in two steady states as in a regular saddle-node bifurcation leading to a splitting of the periodic solution in two heteroclinic orbits. While we expect the global bifurcation to be a SNIPER, there is also the possibility of a homoclinic bifurcation, which also leads to the emergence or destruction of a periodic solution and a diverging period. In this case the amplitude of a periodic solution increases and the trajectory approaches the vicinity of a steady state. At the bifurcation point the periodic solution collides with the steady state, forming a homoclinic orbit. The two possible bifurcations can be distinguished by the scaling of the period with the distance μ to the bifurcation point, while approaching the latter. In

the case of a SNIPER the Period T scales according to $T \propto \frac{1}{\sqrt{\mu}}$ and for a homoclinic bifurcation scales like $T \propto \ln(\mu)$ [31]. However, since the branch of periodic solutions shown in fig. 3.2.15 does not reach the bifurcation point we can not determine the distance to it accurately enough to distinguish both cases.

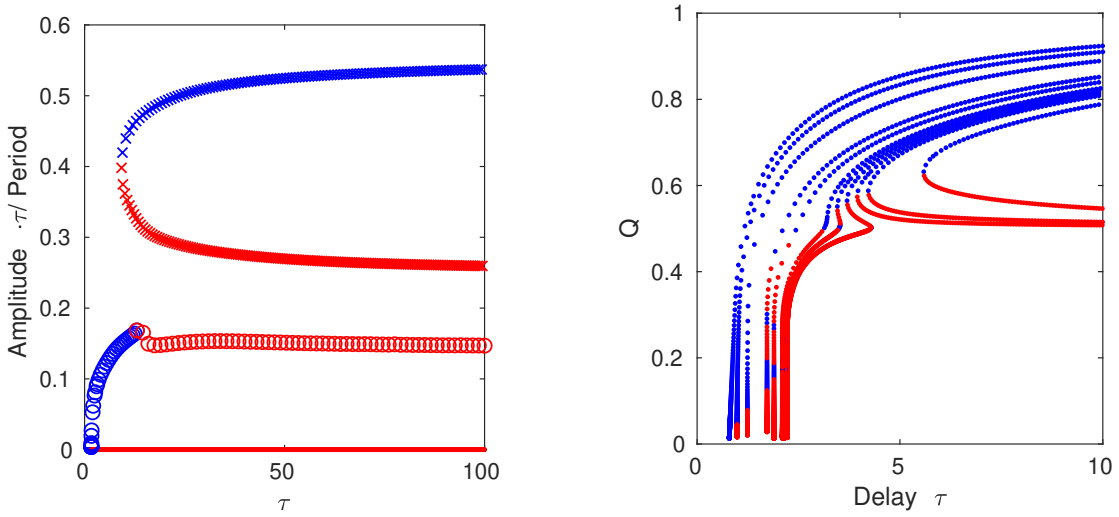

Figure 3.2.16: Left panel: Bifurcation diagram including steady states (dots), oscillations (∘) and periodic solutions (+) away from the saddle-node of steady states for $\Delta = 0.1$, $\psi = 2.84$ and $\chi = 1$. Right panel: Branches of periodic solutions in the (τ, Q) plane with increasing distance from the saddle-node of steady states. Parameters are: $\chi = 1$, $\psi = \pi/2$, $\Delta = [0.7; 0.8; 0.825; 0.85; 0.875; 0.9; 1; 1.1; 1.5; 1.8; 2]$ from right to left. Stable solutions are blue and unstable solutions red in both panels.

Apparently this global bifurcation is not always present as can be seen in the left panel of fig. 3.2.16. Here a bifurcation diagram including steady states (dots), oscillations (∘) and periodic solutions (+) is shown for a different set of parameters ($\Delta = 0.1$, $\psi = 2.84$ and $\chi = 1$) which is not in the vicinity of the saddle-node bifurcation of steady states. In this case the period of the periodic solution does not diverge and there is no indication of a connection between the different solutions, even for large delays. The transition from a global bifurcation shown in the right panel of fig. 3.2.15 and the saddle-node bifurcation of periodic solutions in the left panel of fig. 3.2.16 was further investigated. Multiple branches of periodic solutions were calculated for different distances from the saddle-node bifurcation of the steady states which is at $\Delta = 2$ for the given values of ψ and χ. Periodic solutions in the vicinity of the steady state saddle-node show a global bifurcation while for larger distances the branch deforms and finally shows a regular saddle-node bifurcation for values of $\Delta < 0.825$.

In order to follow the evolution of the bifurcation point in delay τ and feedback strength χ several branches in τ, each for a different value of χ, where calculated. To ensure the divergence, Δ was chosen such that the system is on the border of the steady state saddle-node bifurcation, which is at $\Delta = 1 + \chi \sin(\psi)$. Figure 3.2.17 shows these branches for $\psi = 0$. The left panel shows the diverging part of the branches in Q with a marker at $Q = 0.04$ for each branch which correlates to a period T 25 times bigger than the delay τ and thus can be seen as approximately diverging. The right panel shows the period T of a selection of those branches instead of the topological charge Q. Here the

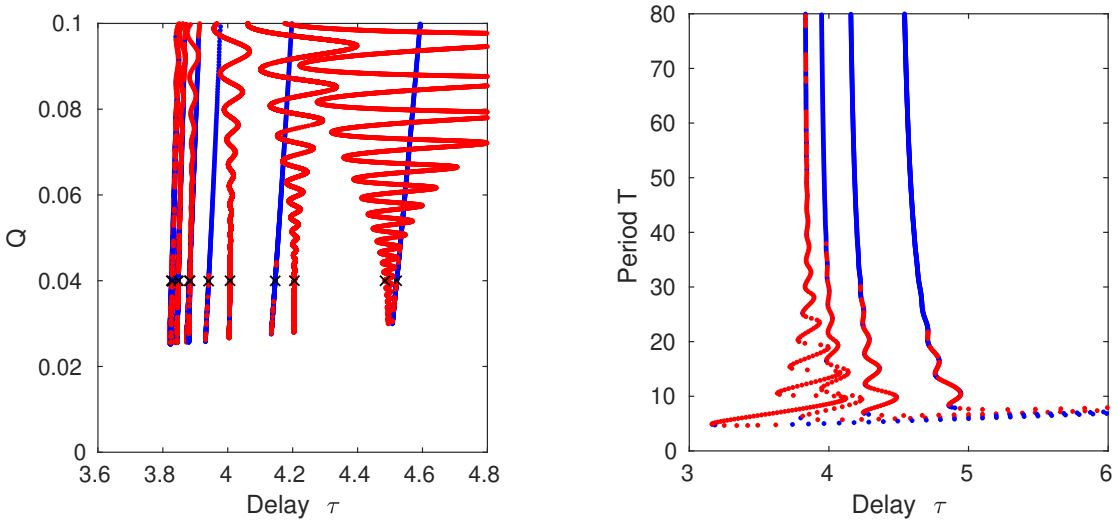

Figure 3.2.17: Determination of the divergence point for different χ in (τ, Q) plane at the saddle-node of steady states and $\psi = 0$, $\Delta = 1$. Feedback strength χ varies from 0.4 to 1.2. Left panel shows the lower end of multiple branches with varying values of χ, while the black crosses indicate approximate divergence at $Q = 0.04$. The right panel shows a selection of the same branches with the period T instead of Q to show the divergence. Stable solutions are blue and unstable solutions red in both panels.

diverging nature becomes more obvious as the branches lead to nearly vertical lines at the diverging points. In addition one can observe that the unstable parts of the branches show a snaking behavior for high feedback strengths. This can possibly lead to a small error in the detection of the diverging point.

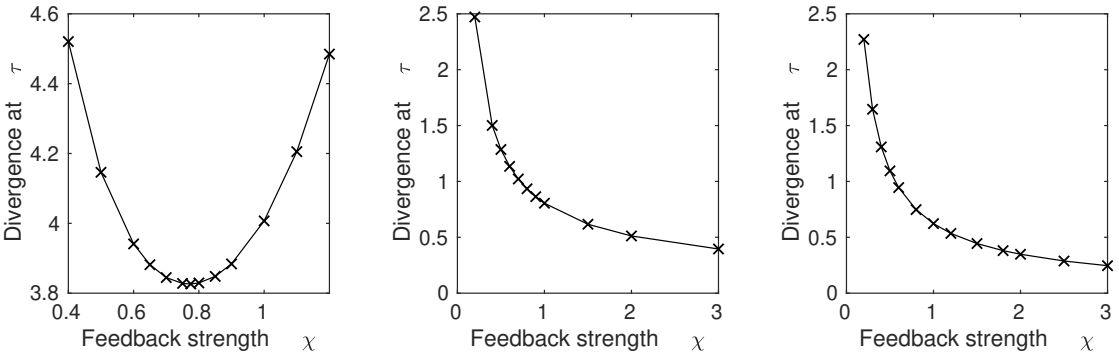

Figure 3.2.18: Dependence of approximated global bifurcation point on χ for different values of ψ. The left panel shows $\psi = 0$, the middle panel $\psi = \pi/2$ and the right panel $\psi = \pi$.

This procedure was repeated for values of $\psi = \pi/2$ and $\psi = \pi$ and the results are shown in fig. 3.2.18. The middle and the right panel look rather similar and seem to approach $\tau = 0$ for $\chi \to \infty$, while diverging for $\chi \to 0$. The left panel showing the results for $\psi = 0$ however looks generally different. The values of τ at which the divergence occurs seem to be generally higher and the relation between delay and feedback strength seem to resemble a parabola $\tau \propto \chi^2$.

In contrast to the local bifurcations explored in section 3.2.2 involving periodic solutions, the bifurcation, leading to the branch of periodic solutions, could be a global one connecting the periodic solutions with nonzero topological charge Q to the background steady state θ_s. Since this bifurcation is neither visible in the linear stability analysis of the steady state nor the periodic solutions the results obtained with the shown approximate method is as close as we can get to following the bifurcation in parameter space.

3.3 Interaction between Localised States

To approximate the interaction of two distant LSs introduced in section 3.2.3 a solution of equation (3.0.1) with multiple LSs is defined as

$$\theta(t) = \theta_s + \sum_i \phi_i(t), \tag{3.3.1}$$

where $\phi_i(t) = \phi(t - x_i(t))$ represent stable orbits from 0 to 2π centered around x_i. The LSs can generally be expanded by exponentials governing the dynamics into and out of the steady state θ_s

$$\phi(t) = \phi(-\infty) + \sum_i f_{i-} e^{\sigma_{i-} t}, \tag{3.3.2}$$

$$\phi(t) = \phi(\infty) + \sum_i f_{i+} e^{\sigma_{i+} t}. \tag{3.3.3}$$

With $\sigma_{i\pm}$ being complex propagation constants and $f_{i\pm}$ the corresponding amplitudes. Note that a real-valued $\sigma_{i\pm}$ leads to a monotonic tail while $\sigma_{i\pm} \in \mathbb{C}$ can lead to oscillatory tails. In order for the solution to remain bounded all coefficients f_{i+} with $\sigma_{i+} > 0$ have to be zero as well as all f_{i-} with $\sigma_{i-} < 0$. In addition, we can assume only the smallest varying exponent having an influence on the far away tails of the LS so that we only consider one $\sigma_\pm$ with the smallest absolute real part, i.e.

$$\phi(t) = \Re\left(a_\pm e^{\sigma_\pm t}\right) \tag{3.3.4}$$

for the approximation of distant tails of a LS going into or out of the steady state, where $a_\pm$ is the amplitude $f_{i\pm}$ corresponding to $\sigma_{i\pm}$ with the smallest absolute real part.
Because we are considering periodic solutions with period $T = \tau + r$, where r is defined as the drift $T - \tau$, we can rewrite Equation (3.0.1) as

$$\frac{\mathrm{d}\theta}{\mathrm{d}t} = \Delta - \sin(\theta(t)) + \chi \sin(\theta(t + r) - \theta(t)). \tag{3.3.5}$$

Inserting the general exponential expansion eq. (3.3.2) or (3.3.3) leads to the expression

$$\sigma_\pm = A + B e^{\sigma_\pm r} \tag{3.3.6}$$

where A and B are the same coefficients as in equation (3.1.3) and (3.1.4). The exponents of the expansion are therefore the solutions of the eigenvalue problem of the LSA, where the delay τ is replaced with a small negative time r, given by the mismatch between delay τ and period T.
If we write the right hand side of the original delayed Adler equation (3.0.1) as

$$\frac{\mathrm{d}\theta_s + \phi(t)}{\mathrm{d}t}\Delta - \sin(\theta_s + \phi(t)) + \chi \sin(\phi(t - \tau) - \phi(t)) = F(\phi(t), \phi(t - \tau)) \tag{3.3.7}$$

one can expand the left hand side of the corresponding dynamic system, describing two LSs, as:

$$\begin{aligned} &\frac{\mathrm{d}(\theta_s + \phi_1(t - x_1(t)) + \phi_2(t - x_2(t)))}{\mathrm{d}t} \\ &= \left(1 - \frac{\mathrm{d}x_1(t)}{\mathrm{d}t}\right)\frac{\mathrm{d}\phi_1(t)}{\mathrm{d}t} + \left(1 - \frac{\mathrm{d}x_2(t)}{\mathrm{d}t}\right)\frac{\mathrm{d}\phi_2(t)}{\mathrm{d}t} \\ &= \left(1 - \frac{\mathrm{d}x_1(t)}{\mathrm{d}t}\right) F(\phi_1(t), \phi_1(t - \tau)) + \left(1 - \frac{\mathrm{d}x_2(t)}{\mathrm{d}t}\right) F(\phi_2(t), \phi_2(t - \tau)) \end{aligned} \tag{3.3.8}$$

and approximate the right hand side around $F(\phi_2(t), \phi_2(t-\tau))$ as:

$$\begin{aligned} & F(\phi_1(t)+\phi_2(t), \phi_1(t-\tau)+\phi_2(t-\tau)) \\ =& F(\phi_2(t), \phi_2(t-\tau)) + \phi_1(t)\frac{\partial}{\partial\phi_1(t)}F(\phi_2(t), \phi_2(t-\tau)) \\ &+\phi_1(t-\tau)\frac{\partial}{\partial\phi_2(t-\tau)}F(\phi_2(t), \phi_2(t-\tau)). \end{aligned} \tag{3.3.9}$$

By using the exponetial approximation of $\phi_1(t)$ and $\phi_1(t-\tau)$ in equation (3.3.4) one can derive the following equation:

$$\begin{aligned} & -\frac{\mathrm{d}x_1(t)}{\mathrm{d}t}\frac{\mathrm{d}\phi_1(t)}{\mathrm{d}t} - \frac{\mathrm{d}x_2(t)}{\mathrm{d}t}\frac{\mathrm{d}\phi_2(t)}{\mathrm{d}t} \\ =& \Re\left(a_+ e^{\sigma_+(t-x_1(t))}\left(\frac{\partial}{\partial\phi_1(t)}F(\phi_2(t), \phi_2(t-\tau)) - \sigma_+\right)\right. \\ &\left. + a_+ e^{\sigma_+(t+r-x_1(t))}\frac{\partial}{\partial\phi_2(t)}F(\phi_2(t), \phi_2(t-\tau))\right). \end{aligned} \tag{3.3.10}$$

When defining a scalar product $(\phi_a, \phi_b) = \int \phi_a^\dagger \phi_b \mathrm{d}t$ using adjoint functions $\phi^\dagger$, defined as solutions of the adjoint problem of the original delayed Adler equation (3.0.1), it is possible to project this equation onto the adjoint eigenvectors. This results in approximate equations of motion for the centers of the LSs of positions $x_1(t)$ and $x_2(t)$:

$$\frac{\mathrm{d}x_2(t)}{\mathrm{d}t} = \Re\left(F_+ e^{\sigma_+(x_2-x_1)}\right), \tag{3.3.11}$$

$$\frac{\mathrm{d}x_1(t)}{\mathrm{d}t} = \Re\left(F_- e^{\sigma_-(x_1-x_2)}\right), \tag{3.3.12}$$

$$\frac{\mathrm{d}a(t)}{\mathrm{d}t} = \Re\left(F_+ e^{\sigma_+ a} - F_- e^{-\sigma_- a}\right). \tag{3.3.13}$$

where $a = x_2 - x_1$ is the distance between the centers of both LSs. The coefficients $F_\pm$ are given by:

$$F_\pm = \frac{\int_{-\infty}^{\infty}\phi^\dagger(s)e^{\sigma_\pm s}\times\left(\frac{\partial}{\partial\phi_1(t)}F(\phi_2(t), \phi_2(t-\tau)) - \sigma_\pm + e^{\sigma_\pm r}\frac{\partial}{\partial\phi_2(t)}F(\phi_2(t), \phi_2(t-\tau))\right)\mathrm{d}s}{\int_{-\infty}^{\infty}\phi^\dagger(s)\dot{\phi}(s)\mathrm{d}s} f_\pm \tag{3.3.14}$$

In order to calculate those coefficients we need an adjoint problem of the initial Adler equation (3.0.1) with which we can obtain adjoint eigensolutions $\phi^\dagger(t)$.
An algorithm calculating the coefficients $F_\pm$ from a `dde-biftool` branch point was supplied by [32], using the definition of the adjoint problem

$$-\dot{v} = a^\dagger(t)v(t) + b^\dagger(t+\tau)v(t+\tau) \tag{3.3.15}$$

of the solution that was linearised around a periodic orbit $\theta_s + \phi(t) + \epsilon u(t)$ leading to

$$\dot{u} = a(t)u(t) + b(t)u(t-\tau). \tag{3.3.16}$$

The eigenfunctions were then calculated using the Implicitly Restarted Arnoldy Method (IRAM) [33].

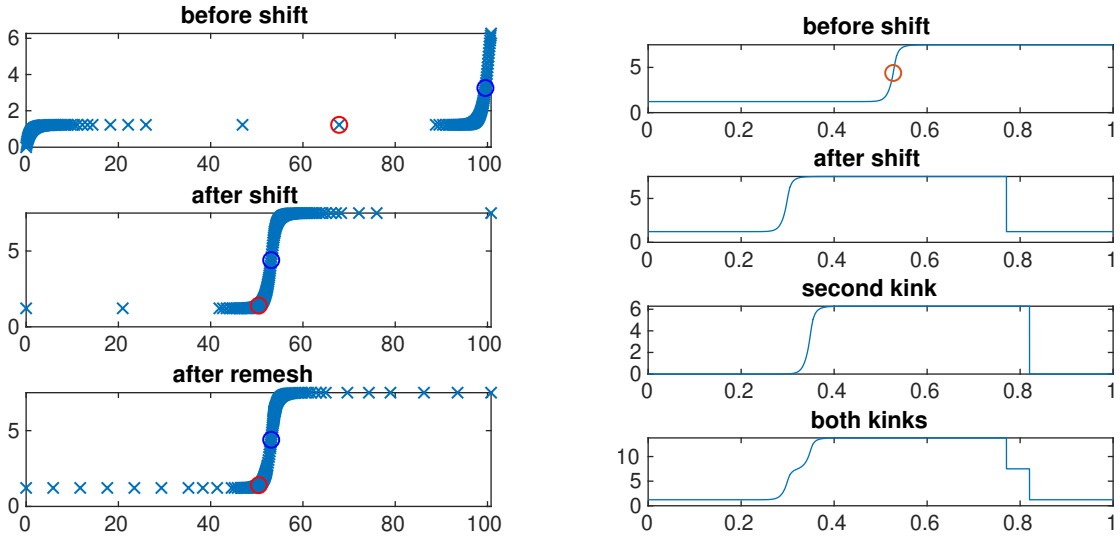

Figure 3.3.1: Preparation of the starting condition for DNS from a profile of a `dde-biftool` branch point. The left panel shows manipulation with `dde-biftool` routines to shift the LS close to the center and remesh the profile. The right panel shows the placement of the LSs to the desired positions and the final profile as sum of multiple shifted LSs.

To test this approach we need to compare the results, given by the reduced eq. of motion (3.3.11) and (3.3.12), with direct numerical simulation (DNS) of the full delayed Adler equation (3.0.1). The history for the integration is put together by adding multiple profiles taken from a branch point out of `dde-biftool`. In order to shift the LS to any desired position we have to switch from the adaptive mesh of `dde-biftool` to a equidistant mesh. The LS can then be positioned by simply circularly shifting the profile. This introduces a 2π jump in θ as can be seen in the right panel of fig. 3.3.1. This discontinuity could be eliminated, but this is not necessary since the system is 2π periodic. After adding multiple profiles, each shifted to the desired position, one has to subtract the background steady state on all but one profiles. The resulting profile is then integrated using a classical Runge-Kutta 4 method.

In order to visualize the interaction between the LSs we use a pseudo-space-time representation as introduced in [9]. This is achieved by cutting the time trace in slices of one period T and rearranging them in a second dimension. This is similar to the approach of multiple timescale analysis, since we display the dynamics happening in one period on one axis and show the slower evolution from one period to the next on the other axis. One example of such a pseudo space time representation can be seen in the top panel of fig. 3.3.2 where two LSs that are close to each other were used as a initial condition. The y-axis represents the fast time scale and goes from 0 to T, while only the region containing the LS is shown. The x-axis displays the round trip number which is, in contrast to the fast scale, a discrete scale. The results of the DNS are displayed in gray scale of $\cos(\theta(t) - \theta_s)$ such that the steady states appear white and the LSs appear in a shade of gray representing the distance to θ_s. The red lines overlaying the diagram are the results of an integration of the reduced system of the centers of each LS using equation (3.3.11) and (3.3.12).

The bottom left panel of fig. 3.3.2 shows a potential for the relative distance between the LSs defined as:

$$V(t) = -\int_t^T a(t')\mathrm{d}t', \tag{3.3.17}$$

where $a(t)$ is given in (3.3.13). The bottom right panel shows the distance between the two LSs obtained from the reduced eq. of motion (3.3.13) and the distance obtained from the DNS of the delayed Adler equation (3.0.1). In addition the widths of both LSs were calculated each round trip using the definition W_+ shown in section 3.2.3.
When comparing the results of the reduced eq. of motion (3.3.11) to (3.3.13) and the DNS in the top panel of fig. 3.3.2 one can generally see a good agreement between the two. However, in the beginning there seems to be a mismatch between the lower red line and the gray scale representation of the lower LS. This can also be seen in the bottom right panel of fig. 3.3.2 where the distance between the LSs shows a different behavior in the DNS and the reduced system. There are two possible reasons of this mismatch that are related to the width of the two LSs which is also shown in the bottom right of fig. 3.3.2. First of all the width of the two LSs seem to be similar to the distance between them while we assumed long distance interaction in the derivation of the reduced eq. of motion (3.3.11) and (3.3.12). After being pushed apart to the point were the distance is greater than the width of the LSs, the reduced eq. of motion (3.3.11) and (3.3.12) seem to agree with the results of the DNS. In addition the two widths of the LSs evolve differently in the beginning of the simulation. While both LSs start with the same width, in the beginning of the DNS one LS gets broader while the other one seems to shrink, before both LS converge to the same width. This shows a asymmetrical deformation of the LSs, which is not accounted for in the derivation of the reduced eq. of motion (3.3.11) and (3.3.12). This deformation could also have its origin in the small starting distance between the LSs.
Figure 3.3.3 shows the results of a DNS of the delayed Adler equation (3.0.1) at different system parameters. While the potential $V(t)$ for the distance between the two LSs in the bottom left of fig. 3.3.3 looks similar to the one in the bottom left of fig. 3.3.2, this time the second LS seems to get pushed by the first one instead of the other way round. There is also a far better agreement between the reduced eq. of motion (3.3.11) and (3.3.12) of LSs and the DNS of the delayed Adler equation (3.0.1) as can be seen in the top as well as the bottom right of fig. 3.3.3. The two LSs start with a width that is considerably smaller than the distance and they do not seem to deform since the width of both LSs stays constant over the whole simulation.
The results shown in fig. 3.3.4 and 3.3.5 display interaction scenarios, in which the LSs are attracted to each other instead of being repelled as can be seen in the potential $V(t)$ shown in the bottom left panels. The two scenarios however, differ in what happens when the two LSs get close to each other. Before going into detail, this is the region where the reduced model is bound to have trouble recreating the interaction as shown in the former cases.
Figure 3.3.4 shows two LSs that approach each other due to the attractive potential seen in the bottom left panel. After about 2000 round trips the attracted LS just disappears leaving the other one behind unaffected. The bottom right panel of fig. 3.3.4 shows an increase in width for one LS while the width of the other vanishes this is caused by both LSs being detected as one big LS for one round trip. The results of the reduced eq. of motion (3.3.11) and (3.3.12) indicated by the red lines in the top panel of fig. 3.3.4 follow the results of the DNS at first but differ from them once the LSs get close

to each other. As can be seen in the potential in the bottom left panel of fig. 3.3.4 there is a stable distance between the two LSs, as indicated by the blue circle at the minimum of the potential. This implies the possibility of a stable molecule bound state of two or possibly more LSs. Since the interaction induced by one LS on the other is not reciprocal, it is possible for the molecule bound state to have a different drift velocity than a single LS. In the analogy of Newtonian particles this is a violation of the third Newtonian law of motion, stating that each force from one particle on another leads to a equal but opposite force, allowing a molecule bound state between two LSs to have a nonzero sum of force.
While the reduced eq. of motion (3.3.11) and (3.3.12) do not represent the results of the DNS for small distances between the LSs, it is nonetheless a very interesting behavior that can be observed in the DNS of the delayed Adler equation (3.0.1) as seen in fig. 3.3.5. Here a similar parameter set than in fig. 3.3.4 was used with a slightly higher feedback phase ϕ and detuning Δ. The simulation starts off the same way as one LS gets pulled to the other but instead of one LS collapsing and the other one continuing unaffected, the two LSs form a molecule bound state with increased drift velocity compared to a single LS. While this behavior fits perfectly to the results of the reduced eq. of motion (3.3.11) and (3.3.12) in fig. 3.3.4, unfortunately the reduced eq. of motion (3.3.11) and (3.3.12) diverge instead of showing a molceule bound state at this parameter set. This mismatch between the reduced eq. of motion (3.3.11) and (3.3.12) and the DNS can again be traced back to the small distance of the LSs and the assumption of long range interaction. A possible improvement of the reduced eq. of motion (3.3.11) and (3.3.12) could be to include higher order terms in the approximation of the tails (3.3.4).

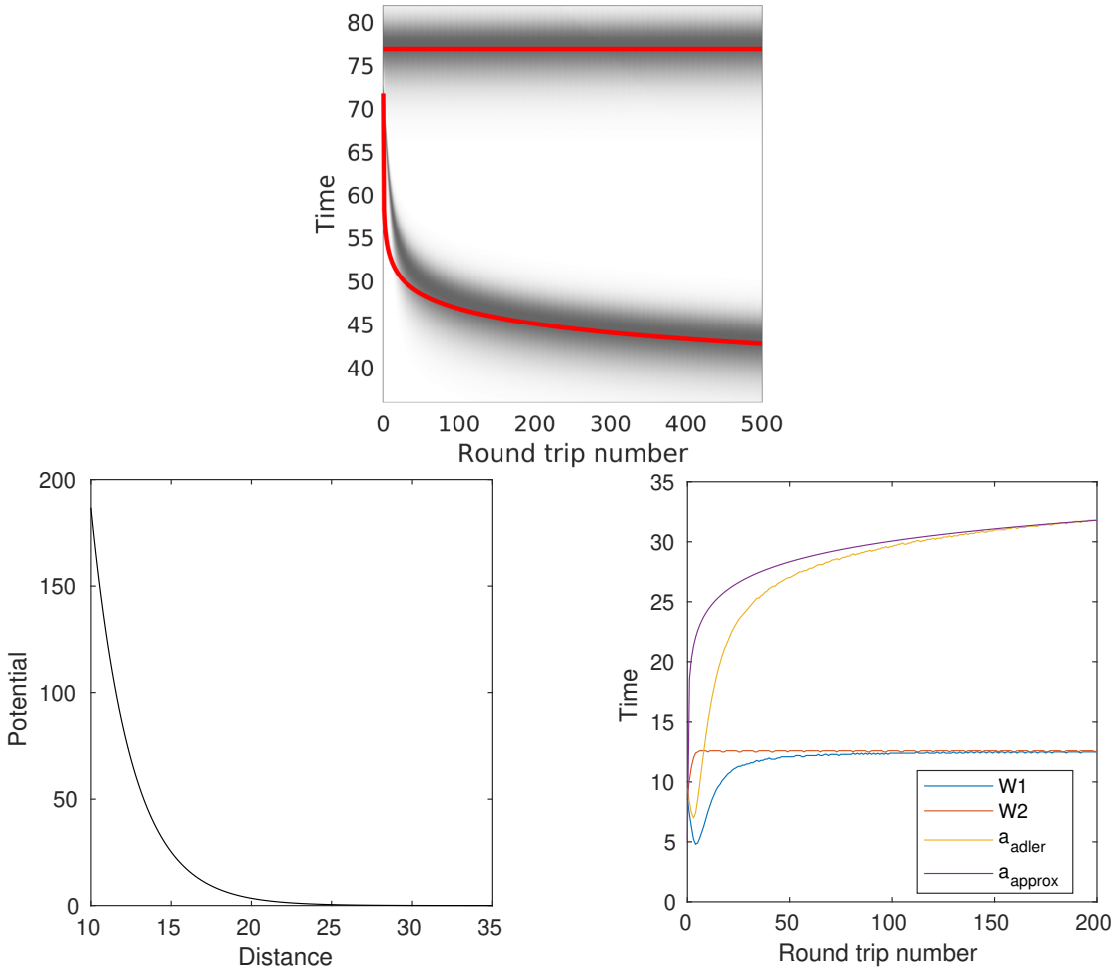

Figure 3.3.2: Top panel: pseudo-space-time representation of DNS of delayed Adler eq. (3.0.1) (gray) and reduced eq. of motion (3.3.11) and (3.3.12) (red).Bottom left panel: potential $V(t)$ given by eq. (3.3.17) for the distance between LSs. Bottom right panel: width of both LSs (W1 and W2) as well as distance between them obtained from DNS (a_{adler}) and the reduced eq. of motion (a_{approx}) respectively. Parameters: $F_+ = 5.6743 \cdot 10^{-4}$; $F_- = -4.1592 \cdot 10^3$; $\sigma_+ = -0.4823$; $\sigma_- = 0.4001$; $\Delta = 0.9974$; $\chi = 2$; $\psi = 1.396$; $\tau = 100$.

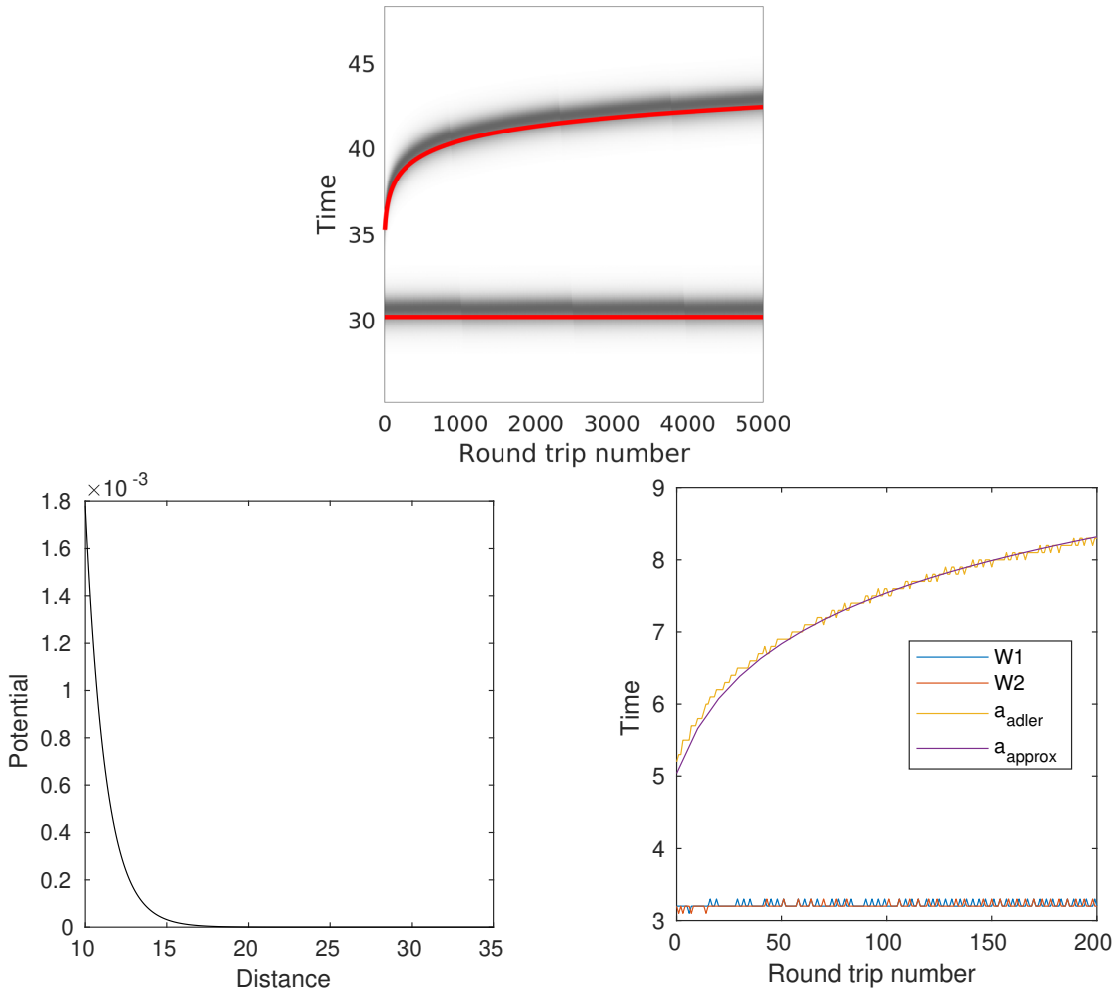

Figure 3.3.3: Top panel: pseudo-space-time representation of DNS of delayed Adler eq. (3.0.1) (gray) and reduced eq. of motion (3.3.11) and (3.3.12) (red).Bottom left panel: potential $V(t)$ given by eq. (3.3.17) for the distance between LSs. Bottom right panel: width of both LSs (W1 and W2) as well as distance between them obtained from DNS (a_{adler}) and the reduced eq. of motion (a_{approx}) respectively. Parameters: $F_+ = 4.8844$; $F_- = 0.0031$; $\sigma_+ = -0.8037$; $\sigma_- = 1.2130$; $\Delta = 0.9393$; $\chi = 0.99$; $\psi = 0$; $\tau = 100$.

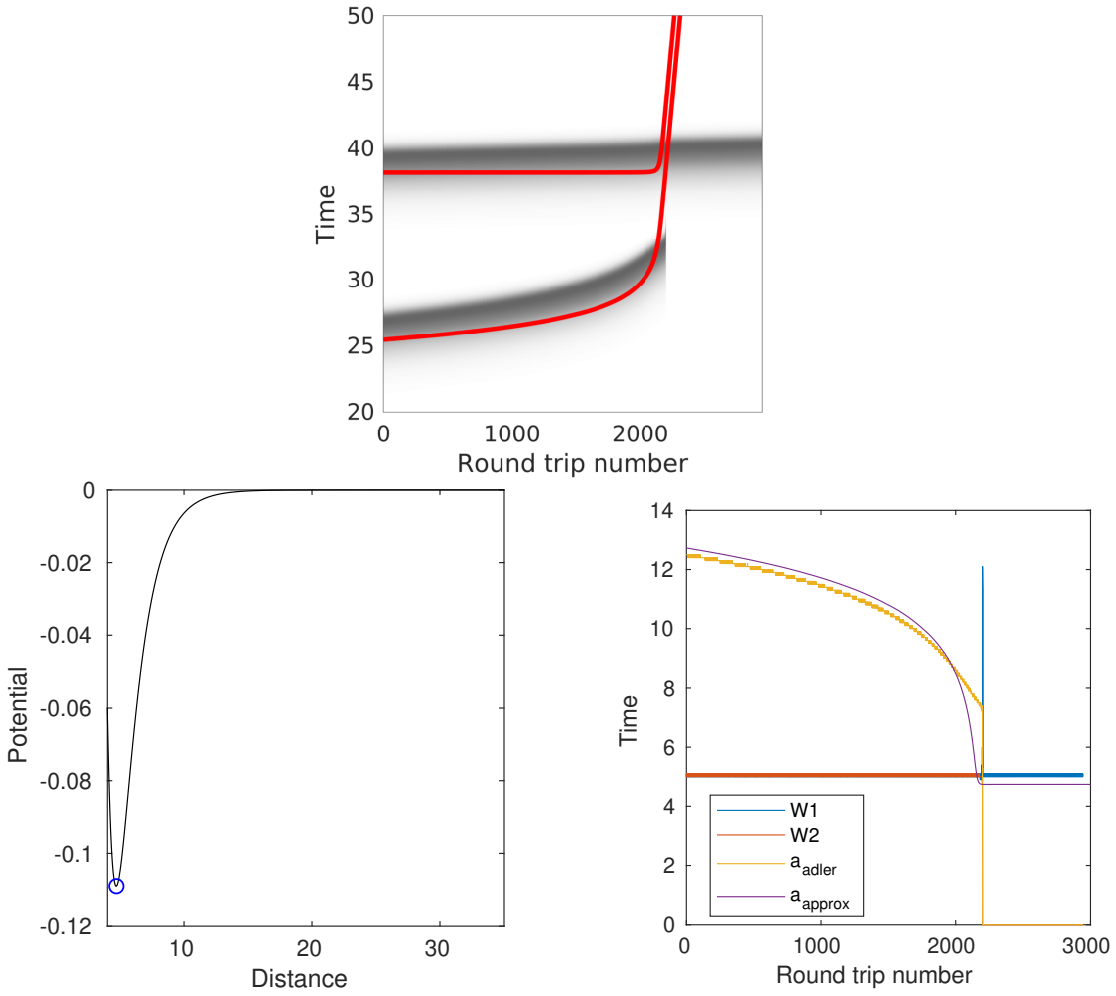

Figure 3.3.4: Top panel: pseudo-space-time representation of DNS of delayed Adler eq. (3.0.1) (gray) and reduced eq. of motion (3.3.11) and (3.3.12) (red).Bottom left panel: potential $V(t)$ given by eq. (3.3.17) for the distance between LSs. Bottom right panel: width of both LSs (W1 and W2) as well as distance between them obtained from DNS (a_{adler}) and the reduced eq. of motion (a_{approx}) respectively. Parameters: $F_+ = 341.55$; $F_- = 2.01$; $\sigma_+ = -1.7034$; $\sigma_- = 0.6201$; $\Delta = 0.8419$; $\chi = 0.99$; $\psi = 0.698$; $\tau = 100$.

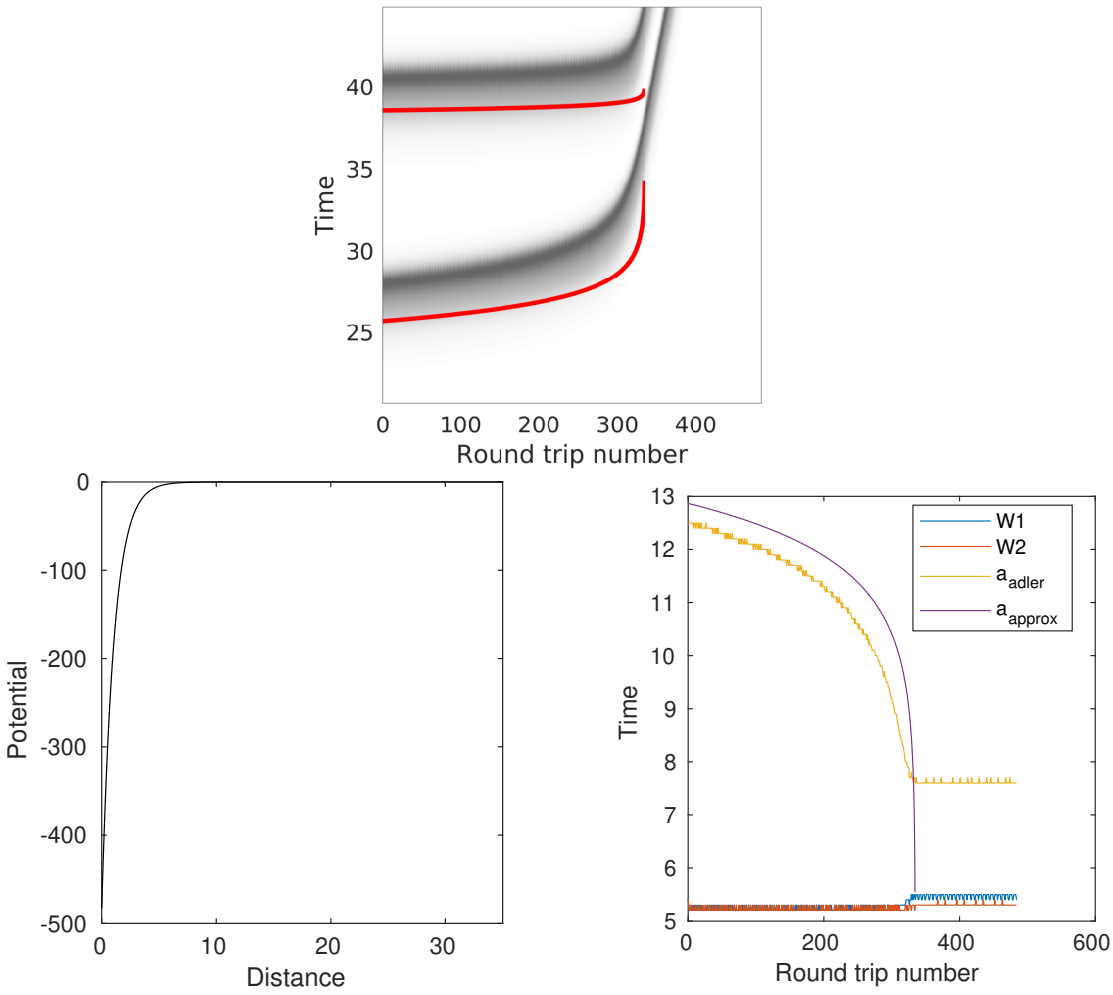

Figure 3.3.5: Top panel: pseudo-space-time representation of DNS of delayed Adler eq. (3.0.1) (gray) and reduced eq. of motion (3.3.11) and (3.3.12) (red).Bottom left panel: potential $V(t)$ given by eq. (3.3.17) for the distance between LSs. Bottom right panel: width of both LSs (W1 and W2) as well as distance between them obtained from DNS (a_{adler}) and the reduced eq. of motion (a_{approx}) respectively. Parameters: $F_+ = 69.017$; $F_- = 536.16$; $\sigma_+ = -0.9032$; $\sigma_- = 0.9203$; $\Delta = 1.099$; $\chi = 0.5$; $\psi = 1.3228$; $\tau = 100$.

3.3.1 Locking

There is a special regime in parameter space, where the exponential tails of the LSs start to oscillate due to a complex range $\sigma_{\pm}$. This region lies in the vicinity of the Hopf instability of the steady states discussed in section 3.1. This opens the possibility for multiple roots of equation (3.3.13) and thus a potential with multiple equidistant minima and maxima. One set of parameters ($\Delta = 0.49$, $\psi = 2.1$, $\chi = 0.99$ and $\tau = 100$) exhibiting this behavior is displayed in fig. 3.3.6, where such a potential can be seen in the top right panel. A series of DNS of the Adler equation (3.0.1) with two LSs at varying distances was performed and can be seen in fig. 3.3.7. One can clearly see the LSs locking to a stable distance, corresponding to the nearest minimum of the potential. The bottom panel of fig. 3.3.6 shows the evolution of the distance between the LSs over multiple round trips. The minima and maxima of the potential are shown in red and blue dashed lines while the distance obtained from the reduced eq. of motion (3.3.11) and (3.3.12) is displayed in black lines. The distance obtained from DNS is also shown in dotted lines.
All distances obtained from the reduced eq. of motion (3.3.11) and (3.3.12) converge to the nearest minimum of the potential which is not surprising since both the potential and the evolution of distance are based on equations (3.3.11), (3.3.12) and (3.3.13). The results of the DNS do not seem to match very good to the reduced eq. of motion (3.3.11) and (3.3.12) in this particular case. While converging to the same distance after many round trips in the four further cases, the two DNS performed in the vicinity of the minimum at a distance of ≈ 15 do not converge to the same value. In addition the dynamics into the stable distance seem to not agree with the reduced eq. of motion (3.3.11) and (3.3.12) at all even in the cases of greater distances between the LSs.
One additional reason for the mismatch between DNS and the reduced eq. of motion (3.3.11) and (3.3.12) was found in the instabilities of the periodic solution discussed in section 3.2.2. The feedback phase of $\psi > \pi/2$ brings the system close to a period doubling regime. A precursor of that period doubling instability can be observed in the DNS of a single LS which is shown in fig. 3.3.8. The time trace is zoomed in to the vicinity of the steady state θ_s, to show the small deviation between the relaxations into the steady state happening every other period. This introduces errors into the reduced model especially if substituting $\theta(t)$ with $\theta(t - T)$.

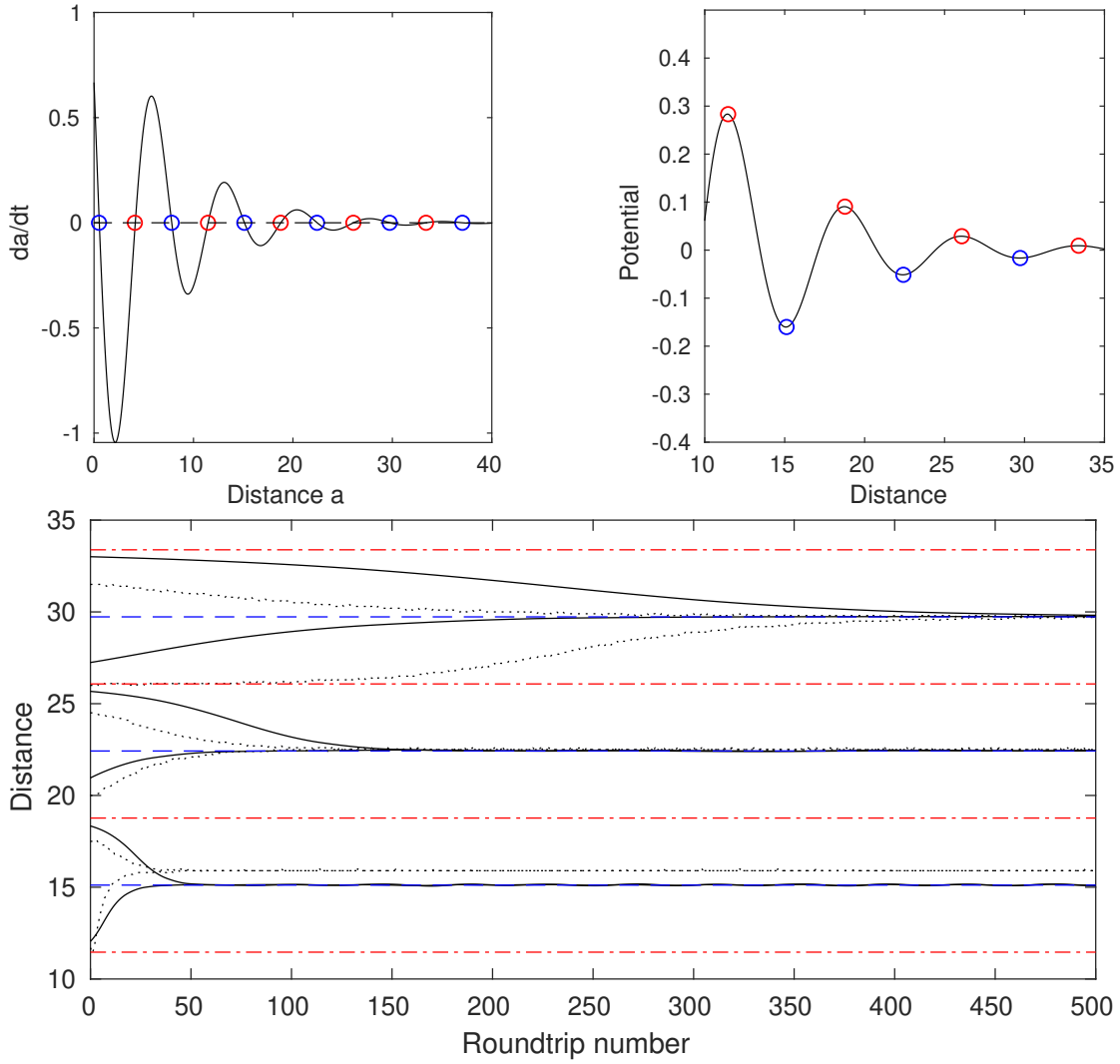

Figure 3.3.6: Nullcline of eq. (3.3.13) and its roots marked in red for downward crossing of zero and blue for upward crossing of zero (left). Potential $V(t)$ for the distance calculated using eq. (3.3.17) (right). Evolution of the distance of two LSs obtained by reduced eq. of motion (3.3.11) and (3.3.12) with different starting conditions. Red and blue dashed lines indicate the roots of Equation (3.3.13) dotted lines are results of DNS of delayed Adler eq. (3.0.1) (bottom).

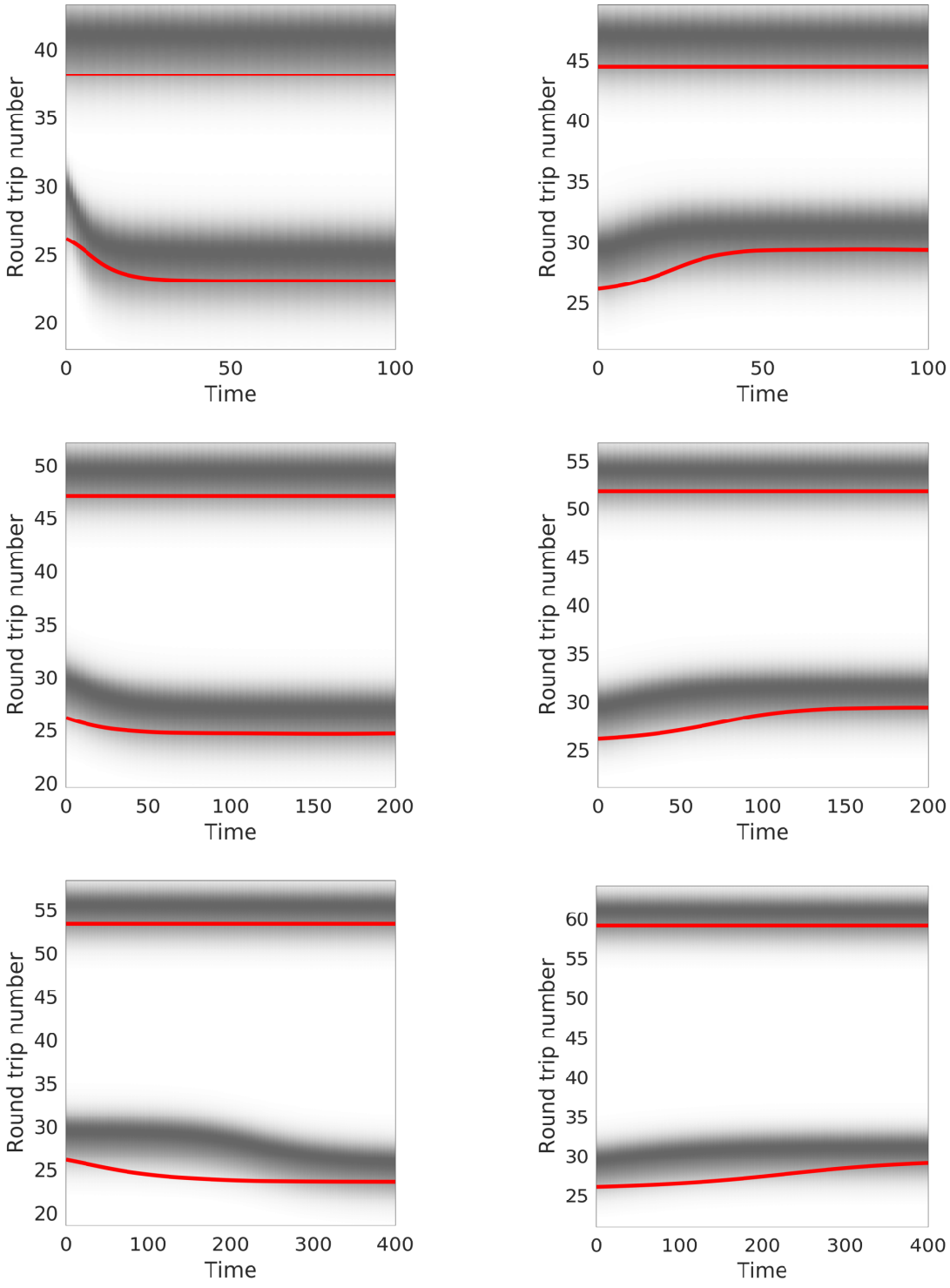

Figure 3.3.7: Pseudo-space-time representation of evolution of two LSs in the locking regime with different starting conditions. The shaded stripes show the DNS of the delayed Adler eq. (3.0.1) while the red lines represent the reduced eq. of motion (3.3.11) and (3.3.12). The initial distances are 12.1 (top left) 18.3 (top right) 21.0 (middle left) 25.7 (middle right) 27.2 (bottom left) 33.0 (bottom right).

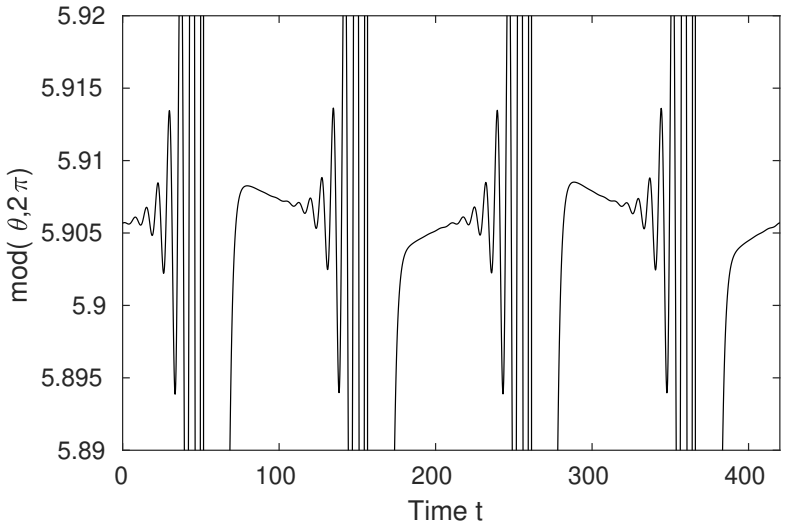

Figure 3.3.8: DNS of delayed Adler eq. (3.0.1) with one LS as initial condition in the locking regime ($\Delta = 0.49$, $\psi = 2.1$, $\chi = 0.99$ and $\tau = 100$) zoomed in on the relaxation in to the steady state θ_s. The difference in behavior on every other period reveals a precursor of a period two instability that was investigated in section 3.2.2

.

3.3.2 Multiple Localised States

In the following we will combine some of the results obtained in the previous sections to show how one could manipulate a system of multiple LSs by changing the systems parameters.
We start the simulation in the regime where LSs can form a molecule bound state, if they are close enough ($\Delta = 1.1$, $\psi = 1.7$, $\chi = 0.99$ and $\tau = 100$), as seen in fig. 3.3.5, with five LSs of varying starting distance. Two of the LSs are close enough to form a molecule bound state that starts to drift. Figure 3.3.9 shows the DNS in pseudo-space-time. Upon reaching another LS the molecule bound state splits in two while one of the LSs forms another molecule bound state with the newly encountered LS. Since the domain is periodic this molecule bound state moves trough it repetitively and interacts with every other LS in the delay line. The LS left behind appears earlier in time than the LS encountered by the molecule bound state because one LS splits off the molecule bound state prior to the new one forming. This essentially shifts all LSs to earlier times on every pass of the molecule bound state through the fast timescale. In fig. 3.3.9 this can be seen between roundtrip 300 and 500 where the molecule bound state passes three LSs with different distances. The three LSs after the pass have the same relative distance to each other as before but appear earlier.

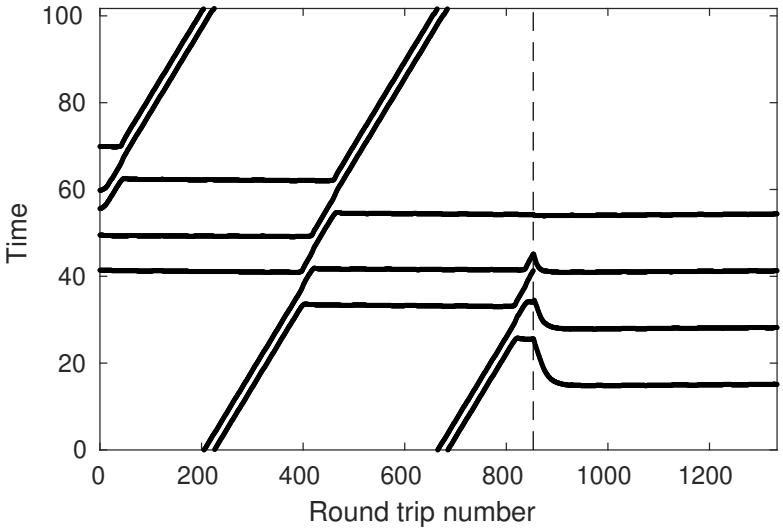

Figure 3.3.9: DNS of delayed Adler eq. (3.0.1) with multiple LSs starting in the regime where two LSs can form a molecule bound state ($\Delta = 1.1$, $\psi = 1.7$, $\chi = 0.99$ and $\tau = 100$). At the dashed line the parameters are changed to a locking regime ($\Delta = 0.6$, $\psi = 2.1$, $\chi = 0.99$ and $\tau = 100$) and the LSs assemble themselves in equal distances. Only the tracked positions of the LSs where plotted instead of the gray scale representation of $\cos(\theta)$.

After round trip 850 the system parameters were changed to $\Delta = 0.6$, $\psi = 2.1$, $\chi = 0.99$ and $\tau = 100$, which is close to the parameters in section 3.3.1 and leads to the same locking behavior. In fig. 3.3.9 this parameter change is indicated by the dashed line. One can clearly see that the LSs organize themselves in an equidistant pattern since every LS locks the next one into a minimum of the induced potential. However there are only four LSs on the right side of the dashed line while the system started with five LSs prior to the parameter change. The missing LS is involved in the molecule bound state specifically the third LS from the top at the dashed line. This annihilation of one LS is most likely

caused by the abrupt change of parameters, which also leads to a sudden change of the shape of a stable LS, combined with the small distance between the LSs due to it being involved in a molecule bound state. This change of shape can not be observed in fig. 3.3.9 since only the current position of each LS defined as $\sin(\theta - \theta_s) = 0.5$ is shown in contrast to the full evolution of $\theta(t)$ as in fig. 3.3.7 or previous pseudo-space-time representations.

3.3.3 Kink-Antikink Interaction

As described in chapter 3.2.1 there exist not only LSs with a positive phase difference of 2π, but also those with a negative phase difference which we called antikinks. While the individual behavior is directly related, and thus not worth to explore, they can coexist for high values of χ as shown in fig. 3.2.5. In this section we will briefly discuss the interactions between kinks and antikinks.

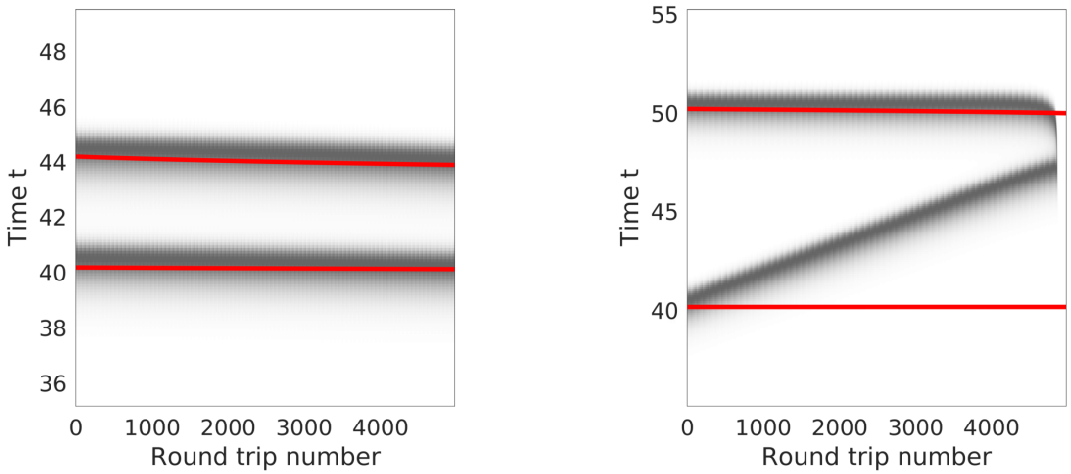

Figure 3.3.10: DNS of a starting profile with a kink and antikink LS at $\chi = 3$, $\tau = 100$ and $\psi = 0$ for no detuning $\Delta = 0$ in the left panel and a small detuning $\Delta = 0.002$ in the right panel.

Since the drift velocity $T - \tau$ of the LS depends on the detuning Δ and mapping the antikinks on the kinks requires to invert θ as well as Δ and ψ the only possibility for a kink and antikink solution to have the same drift velocity $T - \tau$ would be a vanishing detuning $\Delta = 0$. For any nonzero detuning Δ the antikink solution would have the drift velocity corresponding to $-\Delta$. This can also be observed in fig. 3.3.10, where a profile with a kink and antikink solution was simulated with zero detuning and a small detuning of $\Delta = 0.002$ respectively. In the right panel showing the simulation with small detuning one can see the difference in drift velocities leading to a collision of the LSs. As expected the two LS with positive and negative phase difference annihilate each other. This collision of LSs is generally different than the interactions that were shown before, since the relative movement does not originate from effects of one LS on the other but rather is a result of the generally different inherent properties of the LSs. A form of induced interaction can nonetheless be seen in the right panel of fig. 3.3.10 where the two LSs get close and their path gets deformed slightly before annihilation.
In order to approximate the interaction between kinks and antikinks the same way as shown with the kink kink interaction in previous examples, one would have to include the difference in drift velocity $T - \tau$ of the LSs into the derivation of the reduced model.

4 Conclusion and Outlook

In this thesis we have shown that a simple model exhibiting time delay and excitability leads to the existence of topological localised structures. While being derived from a model, describing a experimental setup of injection locked semiconductor lasers with a delayed feedback loop [11], the underlying delayed Adler equation (3.0.1) is simple enough to be applicable to a variety of systems showing both synchronization and delayed feedback.

The steady states of the delayed Adler equation have been described in detail in section 3.1. The instabilities involving the steady states have been approximated in the long delay limit resulting in borders of stability in dependence of the three remaining parameters Δ, ψ and χ describing the detuning, feedback phase and feedback strength respectively (see equations (3.1.9) to (3.1.14)). It was attempted to approximate the discrete eigenvalues of the steady states in order to describe the loss of stability in the additional parameter of time delay τ, leading to the borders given by eq. (3.1.16). In comparison to the exact borders obtained via path-continuation, the qualitative shape and the dependance on τ fits the approximation but the instabilities appear at slightly higher values of τ. The stability of the homogenous steady states plays an important role in the description of LSs since they form the background on which they appear.

Section 3.2 introduces time dependent solutions of excitations that repeat in a period T that is similar to the time delay τ. Those solutions appear to have a stable regime in the vicinity of the steady state saddle node bifurcation and are even stable for values of the detuning Δ beyond the existence of steady states. The topological charge Q in eq. (3.2.1) was defined as the number of 2π phase changes per delay τ, since solutions of approximately half the initial period T were found, which corresponds to more than one excitation appearing in one period. The stable regions of those solutions with different topological charge Q overlap with each other and the steady states, leading to hysteresis. This was shown by integrating the system starting with the steady state while varying the detuning Δ, resulting in different behavior in the forward and backward integration direction.

In addition to positive phase differences there is also the possibility of generating negative 2π-excitations, which occur at negative values of Δ instead of positive (see section 3.2.1). The behavior of those solutions is directly related to those of positive 2π-excitations through arguments of symmetry, which is why they were not explored in detail. One interesting aspect however, is the possible coexistence of positive and negative excitations that was observed for high values of feedback strength χ.

In order to further investigate the periodic solutions a two-parameter bifurcation analysis was performed in section 3.2.2, using Δ and ψ as control parameters. This was accomplished by interpolating multiple branches, that were calculated via one-parameter continuation, into a surface of solutions. The borders of stability could be tracked by `dde-biftool` in Δ and ψ and were displayed together with the surface of solutions in a 3D representation (fig. 3.2.11). While not every instability occurring in the surface was identified and tracked we could reveal the general bifurcation structure of periodic solutions. One important insight is the connection between stable solutions of topological charge Q and $Q+1$ through variation of the feedback phase ψ.

In section 3.2.3 the width and drift of the periodic solutions were investigated. Especially the width is important in the context of localization because the idea of localized excitations is dependent on the solution being approximately in the steady state for

most of the delay time τ. If the width however reaches the magnitude of τ the periodic solutions can no longer be described as localized.
Since all solutions of reoccurring excitations with different topological charge Q seem to be connected the question arises if and how the steady state is also connected to them. This connection was investigated in section 3.2.4 revealing a global bifurcation that occurs for small delay times τ. While this type of bifurcation could not be tracked by `dde-biftool`, we were able to show the influence of feedback strength χ on the divergence of the period T in τ.
Because of the localized nature of the solutions, they should be able to coexist with each other without interaction if the excitations are far enough apart in time. If however, the LSs are close to each other, the residual tails of the relaxation into the steady state can interact and lead to behavior different from isolated LSs. In section 3.3 those interactions are investigated. We were able to show several different interaction scenarios in which the LSs attract or repel each other in different ways. Additionally we were able to derive a reduced model of the long range interaction via a variational method resulting in a ODE system for the centers of mass of two LSs. This reduced model proved to be valid in most cases but failed if both LSs are too close to each other or for parameters where additional instabilities of the periodic solutions are close.
One particularly interesting case of interacting LSs was discussed in section 3.3.1 and 3.3.2 were the locking of several LSs in a self-induced equidistant potential could be observed. This could have applications in reducing crosstalk in the context of LSs as information storing bits in optical communication networks. We note that in [11] the possibility of using topological LSs as phase bits was addressed and it was experimentally shown that they can be individually addressable.
While we could show examples of interacting LSs in different ways at different parameters, a complete mapping of the behavior on parameter space was not achieved and could possibly be of interest for further work. In [34] the dynamics of an ensemble of solitons in a fiber ring resonator were investigated experimentally, while ordered *solid* and unordered *gas* states and phase transitions between them were observed. A more in depth description of the interaction of LSs in the delayed Adler equation (3.0.1) could provide the basis for a thermodynamical model of multiple LSs in a system with large delay.

References

[1] Reinhard Richter and I. V. Barashenkov. Two-Dimensional Solitons on the Surface of Magnetic Fluids. *Physical Review Letters*, 94(18):184503, may 2005.

[2] Mustapha Tlidi, René Lefever, and A. Vladimirov. *On Vegetation Clustering, Localized Bare Soil Spots and Fairy Circles*, volume 751, pages 1–22. Springer Berlin Heidelberg, Berlin, Heidelberg, 2008.

[3] Nail Akhmediev and Adrian Ankiewicz. *Dissipative Solitons: From Optics to Biology and Medicine*, volume 751 of *Lecture Notes in Physics*. Springer Berlin Heidelberg, Berlin, Heidelberg, 2008.

[4] D. J. Korteweg and G. de Vries. XLI. On the change of form of long waves advancing in a rectangular canal, and on a new type of long stationary waves. *The London, Edinburgh, and Dublin Philosophical Magazine and Journal of Science*, 39(240):422–443, may 1895.

[5] Theodore Yaotsu Wu. Nonlinear waves and solitons in water. *Physica D: Nonlinear Phenomena*, 123(1-4):48–63, nov 1998.

[6] C. Schelte, J. Javaloyes, and S. V. Gurevich. Dynamics of temporally localized states in passively mode-locked semiconductor lasers. *Physical Review A*, 97(5):1–15, 2018.

[7] A. Schreiber, B. Thüring, M. Kreuzer, and T. Tschudi. Experimental investigation of solitary structures in a nonlinear optical feedback system. *Optics Communications*, 136(5-6):415–418, apr 1997.

[8] B. Romeira, R. Avó, José M. L. Figueiredo, S. Barland, and J. Javaloyes. Regenerative memory in time-delayed neuromorphic photonic resonators. *Scientific Reports*, 6(1):19510, may 2016.

[9] Giovanni Giacomelli and Antonio Politi. Relationship between Delayed and Spatially Extended Dynamical Systems. *Physical Review Letters*, 76(15):2686–2689, apr 1996.

[10] Stephane Barland, Jorge R. Tredicce, Massimo Brambilla, Luigi A. Lugiato, Salvador Balle, Massimo Giudici, Tommaso Maggipinto, Lorenzo Spinelli, Giovanna Tissoni, Thomas Knödl, Michael Miller, and Roland Jäger. Cavity solitons as pixels in semiconductor microcavities. *Nature*, 419(6908):699–702, oct 2002.

[11] Bruno Garbin, Julien Javaloyes, Giovanna Tissoni, and Stéphane Barland. Topological solitons as addressable phase bits in a driven laser. *Nature Communications*, 6(1):5915, dec 2015.

[12] Andrei G. Vladimirov and Dmitry Turaev. Model for passive mode locking in semiconductor lasers. *Physical Review A*, 72(3):033808, sep 2005.

[13] A. L. Hodgkin and A. F. Huxley. A quantitative description of membrane current and its application to conduction and excitation in nerve. *The Journal of physiology*, 117(4):500–44, aug 1952.

[14] B. Drossel and F. Schwabl. Self Organization in a Forest-Fire Model. *Fractals*, 01(04):1022–1029, dec 1993.

[15] A. Pikovsky, M. Rosenblum, and J. Kurths. *Synchronization: A Universal Concept in Nonlinear Sciences*. Cambridge Nonlinear Science Series. Cambridge University Press, 2003.

[16] Shigeru Shinomoto and Yoshiki Kuramoto. Phase Transitions in Active Rotator Systems Shigeru. *Progress of Theoretical Physics*, 75(5), 1986.

[17] Thomas Erneux. *Applied Delay Differential Equations*, volume 3. Springer New York, New York, NY, 2009.

[18] R. M. Corless, G. H. Gonnet, D. E. G. Hare, D. J. Jeffrey, and D. E. Knuth. On the LambertW function. *Advances in Computational Mathematics*, 5(1):329–359, dec 1996.

[19] M. Lichtner, M. Wolfrum, and S. Yanchuk. The Spectrum of Delay Differential Equations with Large Delay. *SIAM Journal on Mathematical Analysis*, 43(2):788–802, jan 2011.

[20] Serhiy Yanchuk and Giovanni Giacomelli. Spatio-temporal phenomena in complex systems with time delays. *Journal of Physics A: Mathematical and Theoretical*, 50(10):103001, mar 2017.

[21] Rüdiger Seydel. *Practical Bifurcation and Stability Analysis*, volume 5 of *Interdisciplinary Applied Mathematics*. Springer New York, New York, NY, 2010.

[22] Eduard Reithmeier. *Periodic Solutions of Nonlinear Dynamical Systems*, volume 1483 of *Lecture Notes in Mathematics*. Springer Berlin Heidelberg, Berlin, Heidelberg, 1991.

[23] K. Engelborghs, T. Luzyanina, and D. Roose. Numerical bifurcation analysis of delay differential equations using DDE-BIFTOOL. *ACM Transactions on Mathematical Software*, 28(1):1–21, mar 2002.

[24] D. Roose J. Sieber, K. Engelborghs, T. Luzyanina, G. Samaey. DDE-BIFTOOL v. 3.1.1 Manual — Bifurcation analysis of delay differential equations, 2017.

[25] Eusebius J. Doedel. AUTO-07P : Continuation and Bifurcation Software for Ordinary Differential Equations, 2007.

[26] Hannes Uecker, Daniel Wetzel, and Jens D. M. Rademacher. pde2path - A Matlab package for continuation and bifurcation in 2D elliptic systems. aug 2012.

[27] Jan Sieber. Description of extensions ddebiftool_extra_psol and ddebiftool_extra_rotsym, 2017.

[28] Hermann Haken. *Synergetics*, volume 1 of *Springer Series in Synergetics*. Springer Berlin Heidelberg, Berlin, Heidelberg, 1978.

[29] D. Goldobin, M. Rosenblum, and A. Pikovsky. Controlling oscillator coherence by delayed feedback. *Physical Review E*, 67(6):061119, jun 2003.

[30] Niurka R. Quintero, Angel Sánchez, and Franz G. Mertens. Overdamped sine-Gordon kink in a thermal bath. *Physical Review E*, 60(1):222–230, jul 1999.

[31] Steven H. Strogatz. *Nonlinear Dynamics and Chaos*. Westview Press, 2015.

[32] J. Javaloyes. private communication, 2018.

[33] R. B. Lehoucq, D. C. Sorensen, and C Yang. *ARPACK Users' Guide*. Society for Industrial and Applied Mathematics, jan 1998.

[34] F. Mitschke, I. Halama, and A. Schwache. Soliton Gas. *Chaos, Solitons & Fractals*, 10(4-5):913–920, apr 1999.

Acknowledgements

I would like to take this opportunity to thank everybody who was involved in the creation of this thesis.
At first i would like to express my deep gratitude to Priv. Doz. Dr. Svetlana Gurevich for the supervision and guidance during my research and the opportunity to work on this project.
I would like to offer my special thanks to Dr. Julien Javaloyes for the constructive discussions about the topic and the time he took for me.
In addition a thank you to Prof. Dr. Uwe Thiele who agreed to be the second examiner of my thesis.
I would also like to acknowledge the rest of the group *Self-Organization and Complexity* for providing a pleasant work environment and the possibility to frequently hear or give talks about recent work.
Finally i want to thank my friends and family for supporting me during my research.

Declaration of Academic Integrity

I hereby confirm that this thesis on *Topological Localised States in Excitable Delayed Systems* is solely my own work and that I have used no sources or aids other than the ones stated. All passages in my thesis for which other sources, including electronic media, have been used, be it direct quotes or content references, have been acknowledged as such and the sources cited.

_____

(date and signature of student)

I agree to have my thesis checked in order to rule out potential similarities with other works and to have my thesis stored in a database for this purpose.

_____

(date and signature of student)